The Astrophysical Journal, 898:84 (23pp), 2020 July 20 https://doi.org/10.3847/1538-4357/ab9b8d

The 100 pc White Dwarf Sample in the SDSS Footprint

Mukremin Kilic[1], P. Bergeron[2], Alekzander Kosakowski[1], Warren R. Brown[3], Marcel A. Agüeros[4], and Simon Blouin[5]
[1] Homer L. Dodge Department of Physics and Astronomy, University of Oklahoma, 440 W. Brooks St., Norman, OK 73019, USA; kilic@ou.edu
[2] Département de Physique, Université de Montréal, C.P. 6128, Succ. Centre-Ville, Montréal, QC H3C 3J7, Canada
[3] Smithsonian Astrophysical Observatory, 60 Garden Street, Cambridge, MA 02138, USA
[4] Department of Astronomy, Columbia University, 550 West 120th Street, New York, NY 10027, USA
[5] Los Alamos National Laboratory, P.O. Box 1663, Mail Stop P365, Los Alamos, NM 87545, USA
Received 2020 May 13; revised 2020 May 21; accepted 2020 May 30; published 2020 July 27

Abstract

We present follow-up spectroscopy of 711 white dwarfs within 100 pc, and we present a detailed model atmosphere analysis of the 100 pc white dwarf sample in the Sloan Digital Sky Survey footprint. Our spectroscopic follow-up is complete for 83% of the white dwarfs hotter than 6000 K, where the atmospheric composition can be constrained reliably. We identify 1508 DA white dwarfs with pure hydrogen atmospheres. The DA mass distribution has an extremely narrow peak at 0.59 $M_{\odot}$ and reveals a shoulder from relatively massive white dwarfs with $M = 0.7$–$0.9\,M_{\odot}$. Comparing this distribution with binary population synthesis models, we find that the contribution from single stars that form through mergers cannot explain the overabundance of massive white dwarfs. In addition, the mass distribution of cool DAs shows a near absence of $M > 1\,M_{\odot}$ white dwarfs. The pile-up of 0.7–$0.9\,M_{\odot}$ and the disappearance of $M > 1\,M_{\odot}$ white dwarfs is consistent with the effects of core crystallization. Even though the evolutionary models predict the location of the pile-up correctly, the delay from the latent heat of crystallization by itself is insufficient to create a significant pile-up, and additional cooling delays from related effects like phase separation are necessary. We also discuss the population of infrared-faint (ultracool) white dwarfs and demonstrate for the first time the existence of a well-defined sequence in color and magnitude. Curiously, this sequence is connected to a region in the color–magnitude diagrams where the number of white dwarfs with a helium-dominated atmosphere is low. This suggests that the infrared-faint white dwarfs likely have mixed H/He atmospheres.

Unified Astronomy Thesaurus concepts: White dwarf stars (1799); Fundamental parameters of stars (555); Galaxy stellar content (621); Spectrophotometry (1556); Stellar mass functions (1612); Stellar properties (1624)

Supporting material: figure sets, machine-readable tables

1. Introduction

It took astronomers more than half a century to identify the first three white dwarfs and understand their nature (Holberg 2009). Starting with the detection of the companion of Sirius in 1862, only two other white dwarfs, 40 Eridani B and Van Maanen 2, were identified by the 1920s. Interestingly, these white dwarfs reveal a relatively broad mass range, with $M = 0.97 \pm 0.01$, 0.51 ± 0.04, and $0.68 \pm 0.02\,M_{\odot}$, respectively (Holberg et al. 2016).

Thanks to large-scale proper motion (e.g., Luyten 1976) and imaging surveys (e.g., Green et al. 1986), the number of confirmed white dwarfs reached $\sim 2 \times 10^3$ in the late 1990s (McCook & Sion 1987, 1999). The next decade saw a ten-fold increase, thanks to the Sloan Digital Sky Survey spectroscopy (SDSS; Eisenstein et al. 2006; Kleinman et al. 2013; Kepler et al. 2019), and this decade saw another ten-fold increase thanks to the Gaia Data Release 2 astrometry (Gaia Collaboration et al. 2018; Gentile Fusillo et al. 2019). Before Gaia, the only volume-limited and nearly complete white dwarf sample extended only up to 20 pc and included 139 systems (see Holberg et al. 2016; Hollands et al. 2018, and references therein).

Volume-limited surveys provide unbiased estimates of the luminosity and mass functions of white dwarfs, which map the star formation history, the initial–final mass relation (IFMR), the effects of close binary evolution, and the changes in the white dwarf cooling rate as a function of temperature and age. Studying the mass distribution of 298 DA white dwarfs with $T_{\rm eff} \geqslant 13{,}000$ K in the magnitude-limited Palomar–Green Survey (Green et al. 1986), Liebert et al. (2005) found a primary peak at $0.57\,M_{\odot}$ along with a smaller peak from low-mass white dwarfs at $0.4\,M_{\odot}$ and a broad high-mass shoulder centered at $0.78\,M_{\odot}$.

Magnitude-limited surveys are biased against the intrinsically fainter and more massive white dwarfs. Correcting for this bias, Liebert et al. (2005) found that the broad, high-mass component accounts for 22% of the hot DA white dwarfs in their sample, and they suggested binary mergers as a potential explanation for their numbers. White dwarf mass distributions obtained from the SDSS spectroscopy also show similar peaks (for example, see Figure 10 in Kleinman et al. 2013), but the contribution from massive white dwarfs is underestimated given the SDSS spectroscopic survey selection.

Kilic et al. (2018) attempted to constrain the mass distribution using the 100 pc volume-limited white dwarf sample from Gaia. Based on pure hydrogen atmosphere model fits, they found a bimodal mass distribution with peaks at 0.6 and $0.8\,M_{\odot}$, and they estimated a contribution of $\sim$11% from massive white dwarfs. They attributed these to the remnants of main-sequence and post-main-sequence mergers. El-Badry et al. (2018) also found an excess of massive white dwarfs in the SDSS DA white dwarf sample and attributed this excess to a flattened IFMR that favors the formation of massive white dwarfs. On the other hand, Hollands et al. (2018) did not find

Table 1
100 pc White Dwarf Sample in the SDSS Footprint

Object	Gaia Source ID	R.A. (°)	Decl. (°)	ϖ (mas)	$\mu_{\rm R.A.}$ (mas yr^{-1})	$\mu_{\rm Decl.}$ (mas yr^{-1})	G (mag)	$G_{\rm BP}$ (mag)	$G_{\rm RP}$ (mag)
J0000−0403	2447815253423324544	0.04710	−4.05414	22.31 ± 0.22	−117.5 ± 0.4	21.6 ± 0.2	17.80	18.15	17.25
J0000+0132	2738626591386423424	0.17875	1.53930	14.95 ± 0.10	65.6 ± 0.2	−28.4 ± 0.1	16.26	16.29	16.16
J0001+3237	2874216647336589568	0.26821	32.61768	10.15 ± 0.30	−11.3 ± 0.4	−76.9 ± 0.3	19.20	19.53	18.71
J0001−1111	2422442334689173376	0.34738	−11.19932	13.51 ± 0.29	90.3 ± 0.4	−114.6 ± 0.3	18.30	18.47	17.90
J0001+3559	2877080497170502144	0.48816	35.99629	11.66 ± 0.28	38.5 ± 0.3	−57.9 ± 0.2	18.85	19.02	18.35
J0003−0111	2449594087142467712	0.81988	−1.18834	14.07 ± 0.51	99.8 ± 0.6	−12.6 ± 0.4	18.81	19.21	18.20
J0003−0426	2444731325169827200	0.88831	−4.44813	11.62 ± 0.31	−100.3 ± 0.6	−64.2 ± 0.4	18.57	18.78	18.16
J0004−0340	2447889401738675072	1.04394	−3.66918	21.08 ± 0.10	218.7 ± 0.2	−52.9 ± 0.1	16.74	16.90	16.40
J0004+0838	2746843589674667264	1.06322	8.64444	14.22 ± 0.24	67.6 ± 0.6	−52.8 ± 0.3	18.43	18.77	17.95
J0004+1430	2768919442402016896	1.12819	14.50006	11.63 ± 0.49	33.4 ± 1.1	98.5 ± 0.8	19.37	19.78	18.68

Note. The object names, R.A., and decl. are based on the Gaia DR2 epoch of 2015.5.

(This table is available in its entirety in machine-readable form.)

any evidence of an overabundance of massive white dwarfs among the 139 systems in the 20 pc Gaia white dwarf sample.

To constrain the frequency of massive white dwarfs in the solar neighborhood, we initiated a spectroscopic follow-up survey of the 100 pc Gaia white dwarf sample within the SDSS footprint. Here we present the results from this spectroscopic survey. Section 2 describes our sample selection and follow-up observations, whereas Section 3 presents our model atmosphere analysis highlighting the model fits for different spectral types. We discuss the properties of our 100 pc white dwarf sample, including the DA white dwarf mass distribution and the infrared-faint (IR-faint) white dwarfs, in Section 4. We conclude in Section 5.

2. Survey Definition

2.1. Sample Selection

The 100 pc Gaia sample includes more than 10^4 white dwarfs (Gaia Collaboration et al. 2018; Jiménez-Esteban et al. 2018; Kilic et al. 2018; Gentile Fusillo et al. 2019), and it is a challenge to obtain spectroscopy of the entire sample. To make our survey feasible, we limited our follow-up to the SDSS imaging footprint so that we can take advantage of the prior spectroscopy from the SDSS and other surveys that focused on white dwarfs (e.g., Bergeron et al. 1997, 2001; McCook & Sion 1999; Kilic et al. 2006, 2010; Gianninas et al. 2011; Limoges et al. 2015).

To obtain a clean 100 pc white dwarf sample within the SDSS footprint, we used the SDSS Data Release 9 (DR9) catalog matched with Gaia DR2. The SDSS DR9 footprint covers 14,555 square degrees of the northern hemisphere sky, primarily at high $|b| \gtrsim 30°$ Galactic latitudes, as detailed in Ahn et al. (2012). We used the recommendations outlined in Lindegren et al. 2018 to remove non-Gaussian outliers in color and absolute magnitude, and we limited our sample to objects with $>10\sigma$ significant parallax, $G_{\rm BP}$, and $G_{\rm RP}$ photometry. We perform a simple cut in ($G_{\rm BP} - G_{\rm RP}$, $M_{\rm G}$) space to select our sample of white dwarfs. Our selection is optimized for reliability rather than completeness; it keeps isolated white dwarfs and unresolved double degenerates, but removes the majority of the white dwarf + main-sequence binaries.

For completeness, we provide the Astronomical Data Query Language (ADQL) query that we used to define our sample in the Appendix. This query returns 4016 white dwarfs within 100 pc and the SDSS footprint. Table 1 presents the Gaia source ID, coordinates, parallax, proper motions, and magnitude for each object.

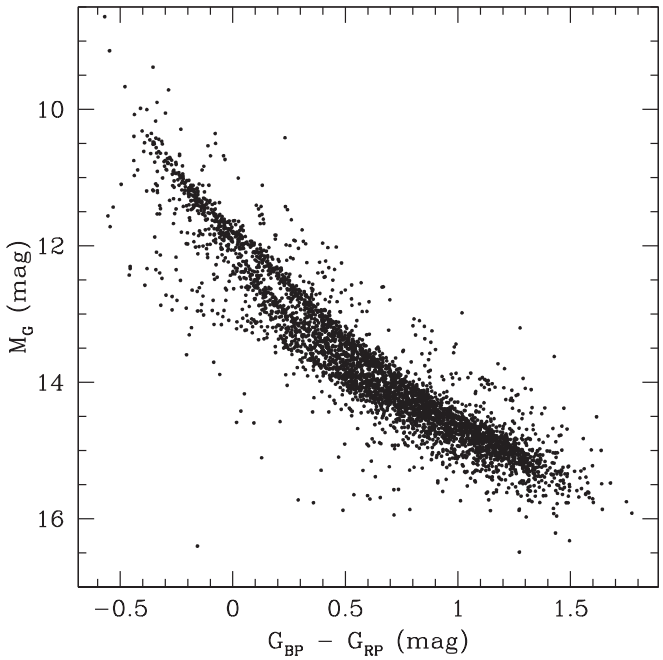

Figure 1. Color–magnitude diagram showing the 100 pc Gaia white dwarf sample within the SDSS footprint. This sample contains 4016 white dwarfs with G magnitudes ranging from 12.1 to 20.6. The bifurcation in the white dwarf sequence due to the atmospheric composition (Bergeron et al. 2019) is clearly visible.

Figure 1 shows these sources in a Gaia color–magnitude diagram. The white dwarf sequence extends from $M_G = 8.6$ to 16.5 mag, with the apparent G magnitudes ranging from 12.1 to 20.6. The split in the white dwarf sequence due to the atmospheric composition is clearly visible (Bergeron et al. 2019).

We cross-matched this sample with the SDSS DR14 spectroscopic catalog (Kepler et al. 2019) and found 1045 white dwarfs with SDSS spectra. We found spectroscopy for 119 additional white dwarfs in Kilic et al. (2006, 2010), 345 objects in the papers by the Montréal group (e.g., Limoges et al. 2015), and 26 objects with data from the Supernovae Type Ia Progenitor Survey (Napiwotzki et al. 2001). We found spectral types for 117 additional objects in the literature (Dufour et al. 2017).

Table 2
Observation Details

Telescope	Instrument	Grating	Slit (″)	Resolution (Å)	λ (Å)	Targets
FLWO 1.5 m	FAST	300 l mm^{-1}	1.5	3.6	3500–7400	23
		600 l mm^{-1}	1.5	2.3	3550–5530	158
MDM 2.4 m	OSMOS	Blue VPH	1.2	3.3	3975–6865	158
APO 3.5 m	DIS	R300	1.5	6.4	5500–9200	107
		B400	1.5	5.2	3400–5500	7
6.5 m MMT	Blue Channel	500 l mm^{-1}	1–1.25	3.8–4.8	3700-6850	233
		300 l mm^{-1}	1–1.25	6.5–8.1	3200–7620	51
Gemini South	GMOS	B600	1.0	5.5	3670–6810	21

Note. DIS B400 + R300 observations were obtained simultaneously.

2.2. Spectroscopic Survey

Spectral typing of white dwarfs based on low-resolution spectroscopy is relatively easy for stars hotter than about 6000 K. This is because hydrogen lines are clearly visible at these temperatures. Hence, the absence or presence of Hα or Hβ is usually sufficient to constrain the atmospheric composition. Helium lines are visible for white dwarfs hotter than 11,000 K, and additional lines from C_2, Ca, and Mg are also visible in DQ and DZ white dwarfs, respectively. Hydrogen lines disappear below about 5000 K, and the majority of the white dwarfs below this temperature show featureless spectra, or DC spectral type. Hence, optical spectroscopy is not useful for constraining the atmospheric composition of cooler white dwarfs, unless they are metal-rich. Therefore, we limit our spectroscopic follow-up survey to white dwarfs with $T_{\rm eff} \geqslant 6000$ K, where our data can reliably constrain the atmospheric composition.

We obtained optical spectroscopy of 711 white dwarfs using the 1.5 m Fred Lawrence Whipple Observatory (FLWO) telescope, the MDM Hiltner 2.4 m telescope, the Apache Point Observatory (APO) 3.5 m telescope, the 6.5 m Multiple Mirror Telescope (MMT), and the 8 m Gemini South telescope. Table 2 presents the details of our observing program, including the instrument configuration and the number of targets observed at each telescope.

At the FLWO 1.5 m telescope, we used the FAST spectrograph (Fabricant et al. 1998) with either the 600 l mm^{-1} or 300 l mm^{-1} grating and the 1.″5 slit to obtain spectroscopy of 81 targets with spectral resolutions of 2.3 and 3.6 Å over the wavelength ranges 3550–5530 Å and 3500–7400 Å, respectively. These observations were done between 2019 January and 2020 February. We found spectroscopy data for 100 additional targets in the FAST archive (Tokarz & Roll 1997).

At the MDM 2.4 m telescope, we used the OSMOS spectrograph (Martini et al. 2011) with the Blue VPH grism and the 1.″2 inner slit to obtain spectroscopy of 158 targets with a spectral resolution of 3.3 Å over the wavelength range 3975–6865 Å. These observations were done between 2018 December and 2019 November as part of the MDM OSMOS queue.

At the APO 3.5 m telescope, we used the Dual Imaging Spectrograph (DIS) with the B400 + R300 gratings and a 1.″5 slit to obtain spectroscopy of 107 targets with spectral resolutions of 5.2 and 6.4 Å in the blue and red channels, respectively. The blue and red channels cover the wavelength ranges 3400–5500 and 5500–9200 Å, respectively. These observations were done between 2018 November and 2019 September. Unfortunately, the DIS blue channel suffered from contamination problems soon after our observing program started, and only seven of our targets have DIS blue channel data available.

At the 6.5 m MMT, we used the Blue Channel Spectrograph (Schmidt et al. 1989) with the 500 l mm^{-1} grating and a 1″ or 1.″25 slit to obtain spectroscopy of 233 targets over the wavelength range 3700–6850 Å with spectral resolutions of 3.8 and 4.8 Å, respectively. We obtained additional observations of 51 stars using the 300 l mm^{-1} grating, which provided spectra from the atmospheric cutoff (3200 Å) to 7620 Å with resolutions of 6.5 and 8.1 Å for the 1″ and 1.″25 slits, respectively. These observations were done between 2018 November and 2019 October.

At the 8 m Gemini South telescope, we used the Gemini Multi-Object Spectrograph (GMOS) with the B600 grating and a 1″ slit to obtain spectroscopy of 21 targets as part of the queue program GS-2020A-Q-222. Unfortunately, our program was cut short by the COVID-19 pandemic, which prohibited observations of additional targets.

Our Gemini observations were done between UT 2020 January 21 and March 7. We binned the CCD by 4 × 4 to reduce the read-out time. This setup provided spectra over the wavelength range 3670–6810 Å, with a resolution of 2 Å per pixel. GMOS on Gemini has three CCDs, with gaps between them. Our observing setup leads to gaps in spectral coverage between 4677–4703 and 5737–5765 Å. These gaps can be eliminated by obtaining multiple exposures with different central wavelength configurations of the grating. Because these gaps have no impact on our spectral classification, and in order to save telescope time, we did not dither in wavelength to eliminate these gaps.

We reduced the data from all five telescopes using standard IRAF routines. About two dozen targets were observed on more than one telescope, and several spectra with low signal-to-noise ratios were also omitted, resulting in a final sample of 711 objects with new spectroscopy data. Of these, 477 are DA, 6 are DB, 195 are DC, 7 are DQ, 27 are DZ, and 1 is a dwarf nova. Two targets are likely magnetic white dwarfs with uncertain spectral types (DAH or DBH) and are included in both the DA and DB samples.

The use of many different telescope and instrument combinations with different resolving powers can lead to systematic uncertainties in the physical parameters derived using the spectroscopic method (Liebert et al. 2005). Here we do not use the spectroscopic method. We use the photometric method instead (see below), and we rely only on Gaia parallaxes and SDSS and Pan-STARRS photometry. Hence, the multiple telescope and instrument combinations have no

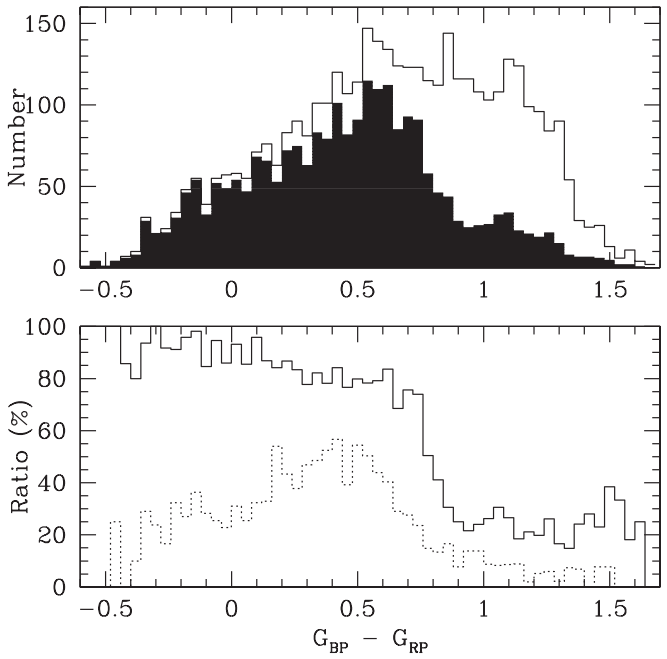

Figure 2. Color distribution of our 100 pc white dwarf sample in the SDSS footprint (solid line, top panel), along with the number of objects with follow-up spectroscopy (shaded histogram). The ratio of the two, that is, the completeness level of the spectroscopic follow-up, is shown as the solid line in the bottom panel. The dotted line shows the completeness of the SDSS spectroscopy only.

impact on the physical parameters derived in our analysis. We simply use each spectrum to confirm the spectral type and to constrain the atmospheric composition of each white dwarf.

The top panel in Figure 2 shows the color distribution of the entire 100 pc white dwarf sample in the SDSS footprint (solid line) and that of the objects with spectroscopy (shaded histogram). The bottom panel shows the completeness of the spectroscopic follow-up.

Combining our data with spectroscopy available in the literature, we have spectral classifications for 2361 (59%) of the 4016 white dwarfs in our sample. Given our survey selection bias for $T_{\rm eff} \geqslant 6000$ K objects, our spectroscopic follow-up is significantly more complete for hotter stars. A $\log g = 8$ pure hydrogen atmosphere white dwarf is predicted to have $G_{\rm BP} - G_{\rm RP} = 0.734$ mag at 6000 K. There are 2213 white dwarfs bluer than that color in our sample, including 1838 with spectra. Hence, our spectroscopic follow-up is 83% complete for white dwarfs hotter than about 6000 K.

3. Model Atmosphere Analysis

3.1. Fitting Method

We use the photometric technique as detailed in Bergeron et al. (2019), who demonstrated that the SDSS *ugriz* photometric system or a combination of SDSS *u* and the Panoramic Survey Telescope and Rapid Response System (Pan-STARRS, Chambers et al. 2016) *grizy* photometry yields accurate parameters. Bergeron et al. (2019) also found that the Pan-STARRS photometry is superior to the SDSS photometry for white dwarf model atmosphere analysis. We follow the same approach and use the SDSS *u* and Pan-STARRS *grizy* photometry in our analysis.

We convert the observed magnitudes into average fluxes using the appropriate zero points, and we compare with the average synthetic fluxes calculated from model atmospheres with the appropriate chemical composition. A χ^2 value is defined in terms of the difference between observed and model fluxes over all bandpasses, properly weighted by the photometric uncertainties, which is then minimized using the nonlinear least-squares method of Levenberg–Marquardt (Press et al. 1986) to obtain the best-fitting parameters. The uncertainties of each fitted parameter are obtained directly from the covariance matrix of the fitting algorithm, while the uncertainties for all other quantities derived from these parameters are calculated by propagating in quadrature the appropriate measurement errors.

We fit for the effective temperature and the solid angle, $\pi(R/D)^2$, where R is the radius of the star and D is its distance. Since the distance is precisely known from Gaia parallaxes, we can constrain the radius of the star directly, and therefore the mass based on the evolutionary models for white dwarfs. The details of our fitting method, including the model grids used, are further discussed in Bergeron et al. (2019) and Genest-Beaulieu & Bergeron (2019). Here we supplement our model grid with the updated DZ and DQ white dwarf models from Blouin et al. (2018a) and Blouin et al. (2019). Since all of our targets are within 100 pc, we do not correct for reddening.

3.2. DA White Dwarfs

Figures 3 and 4 show our methodology for spectral classification based on model fits to four DA white dwarfs identified in this work. We picked these four stars to also demonstrate the observing setup differences between the different telescopes.

For each star, the top panel shows the SDSS *u* and Pan-STARRS *grizy* photometry (error bars) along with the predicted fluxes from the best-fitting pure hydrogen (filled dots) and pure helium (open circles) atmosphere models. The labels in the same panel give the Gaia Source ID, object name based on Gaia DR2 coordinates (for example J0100−2021 for the top left panel in Figure 3), and the photometry used in the fitting: *ugrizy* means SDSS *u* + Pan-STARRS *grizy* while *ugriz* means SDSS *ugriz*. Some filters were omitted in a few cases where for example they were contaminated by an M dwarf companion.

The middle panel, here and in the following figures, always shows the predicted spectrum based on the pure hydrogen solution, along with the observed Hα or Hβ profiles depending on the wavelength coverage of the observations. Note that we do not fit the spectroscopy data here. Instead, we simply overplot the predicted hydrogen line profile (red line) from the photometric fit to see if a given spectrum is consistent with a pure hydrogen atmosphere composition. The spectral type of each object is also given in the middle panel, along with a temperature index based on $50{,}400/T_{\rm eff}$. The bottom panel shows a broader spectral range for each star revealing the presence of additional Balmer lines in the blue, if such data are available.

J0010−2021 (Figure 3, left panels) is a relatively warm DA with several Balmer lines visible in its FAST spectrum and a significant Balmer jump also visible in the *u* and *g* photometry. The photometry and Gaia parallax indicate a pure H atmosphere with $T_{\rm eff} = 10{,}049 \pm 57$ K and $M = 0.554 \pm 0.009\,M_{\odot}$. The predicted H$\alpha$ line profile for these parameters provides an excellent match to the observed spectrum, indicating that this is a white dwarf with a pure hydrogen atmosphere.

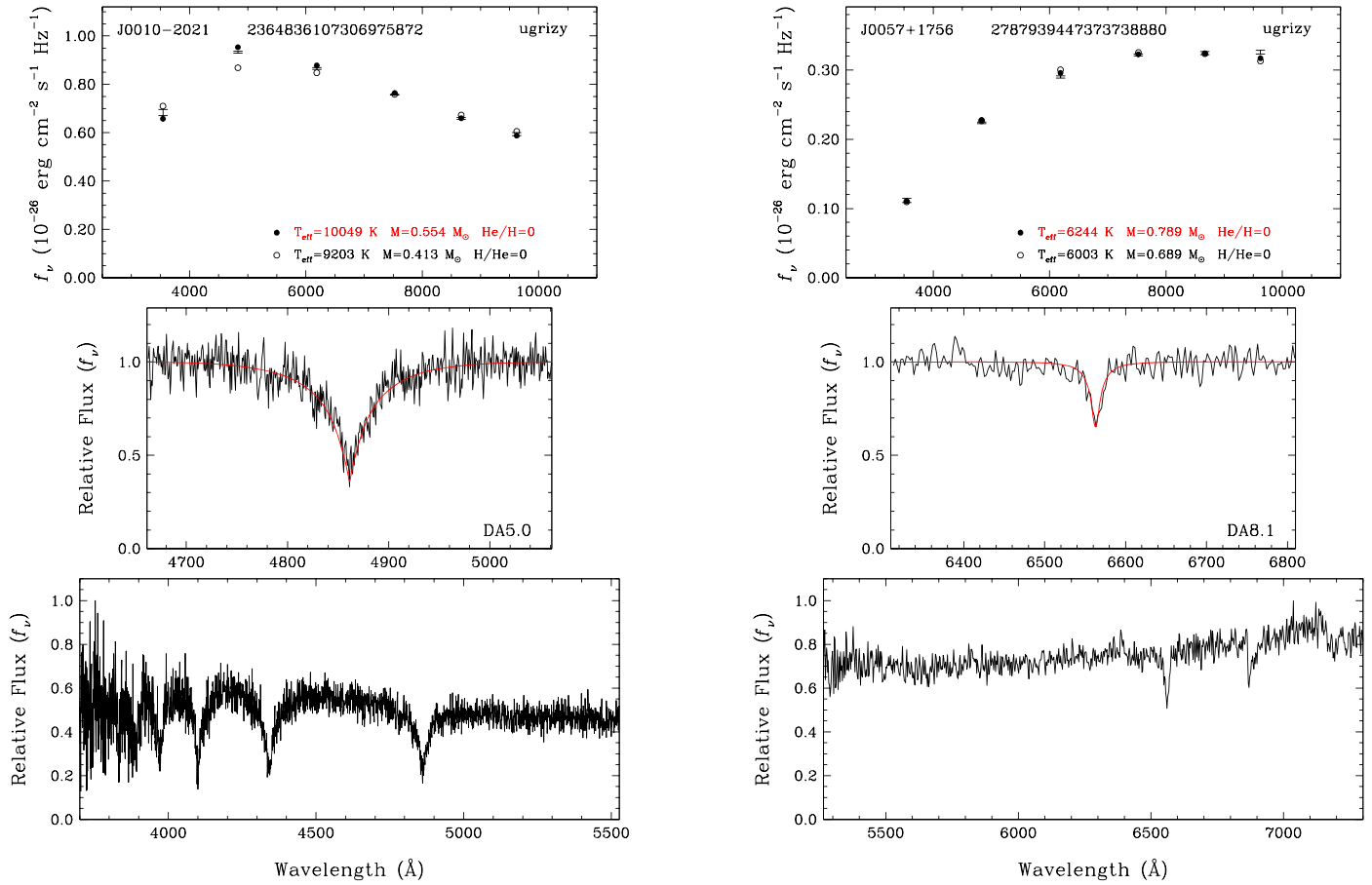

Figure 3. Model fits to two new DA white dwarfs observed at the FLWO 1.5 m and APO 3.5 m telescopes. The top panels show the best-fitting pure hydrogen (filled dots) and pure helium (open circles) atmosphere white dwarf models to the photometry (error bars). Each object is labeled based on its Gaia Source ID, object name based on Gaia DR2 coordinates, and the photometry used in the fitting: *ugrizy* means SDSS u + Pan-STARRS *grizy* while *ugriz* means SDSS *ugriz*. The atmospheric parameters of the favored solution are highlighted in red. The middle panels, here and in the following figures, always show the predicted spectrum (red lines) based on the pure hydrogen solution. The bottom panels show a broader wavelength range for each instrument, revealing additional Balmer lines in the blue for one of these targets. All of the DA white dwarfs are available in the figure set. It has 1553 components.

(The complete figure set (1553 images) is available.)

J0057+1756 (Figure 3, right panels) is a cooler DA white dwarf with no significant Balmer jump visible in its photometry. The best-fitting pure hydrogen atmosphere solution has $T_{\rm eff} = 6244 \pm 29$ K and $M = 0.789 \pm 0.011\,M_{\odot}$. Even though our APO data lack blue coverage for this object, the predicted Hα line profile from the photometric fit matches the observed spectrum, indicating that this is also a white dwarf with a pure hydrogen atmosphere. Note that we did not correct for telluric features, and the atmospheric B-band (6860–6890 Å) is visible in our APO data.

Hydrogen lines become weaker with cooler temperatures. J0031+2218 (Figure 4, left panels) is a cool DA white dwarf with only Hα and Hβ lines visible in our MDM spectrum. The best-fitting pure hydrogen atmosphere solution with $T_{\rm eff} = 6056 \pm 23$ K and $M = 0.629 \pm 0.009\,M_{\odot}$ provides an excellent match to the observed Hα line profile.

J1301−0235 (Figure 4, right panels) is a slightly warmer and more massive ($M = 1.079 \pm 0.029\,M_{\odot}$) DA white dwarf observed at Gemini. The quantum efficiency correction for the three GMOS CCDs is not perfect, resulting in slightly elevated flux levels for the reddest CCD with coverage beyond 5765 Å. This has no impact on our spectral typing. Hα through Hδ are visible in our Gemini spectrum of J1301−0235, and the photometric solution provides a good match to the Hα line profile, indicating that this is also a white dwarf with a pure hydrogen atmosphere.

We present the figures for only four DA white dwarfs here. However, our model fits for all of the spectroscopically confirmed DA white dwarfs in our sample can be found in the online version of this article.

We present the physical parameters of all DA white dwarfs in our sample best explained by pure hydrogen atmosphere models in Table 3. The small errors reported in this table represent the fact that both the photometric and parallax uncertainties are extremely small in most cases. Modern magnitude measurements such as SDSS or Pan-STARRS are quoted with extremely small uncertainties, sometimes as small as millimagnitudes. However, as discussed in detail by Bergeron et al. (2019), even though the photometric technique yields precise parameters, the true accuracy of the method is most likely dominated by the conversion from magnitudes to average fluxes (Holberg & Bergeron 2006). For example, while the Pan-STARRS photometric system attempts to be as close as possible to the AB magnitude system, the Pan-STARRS

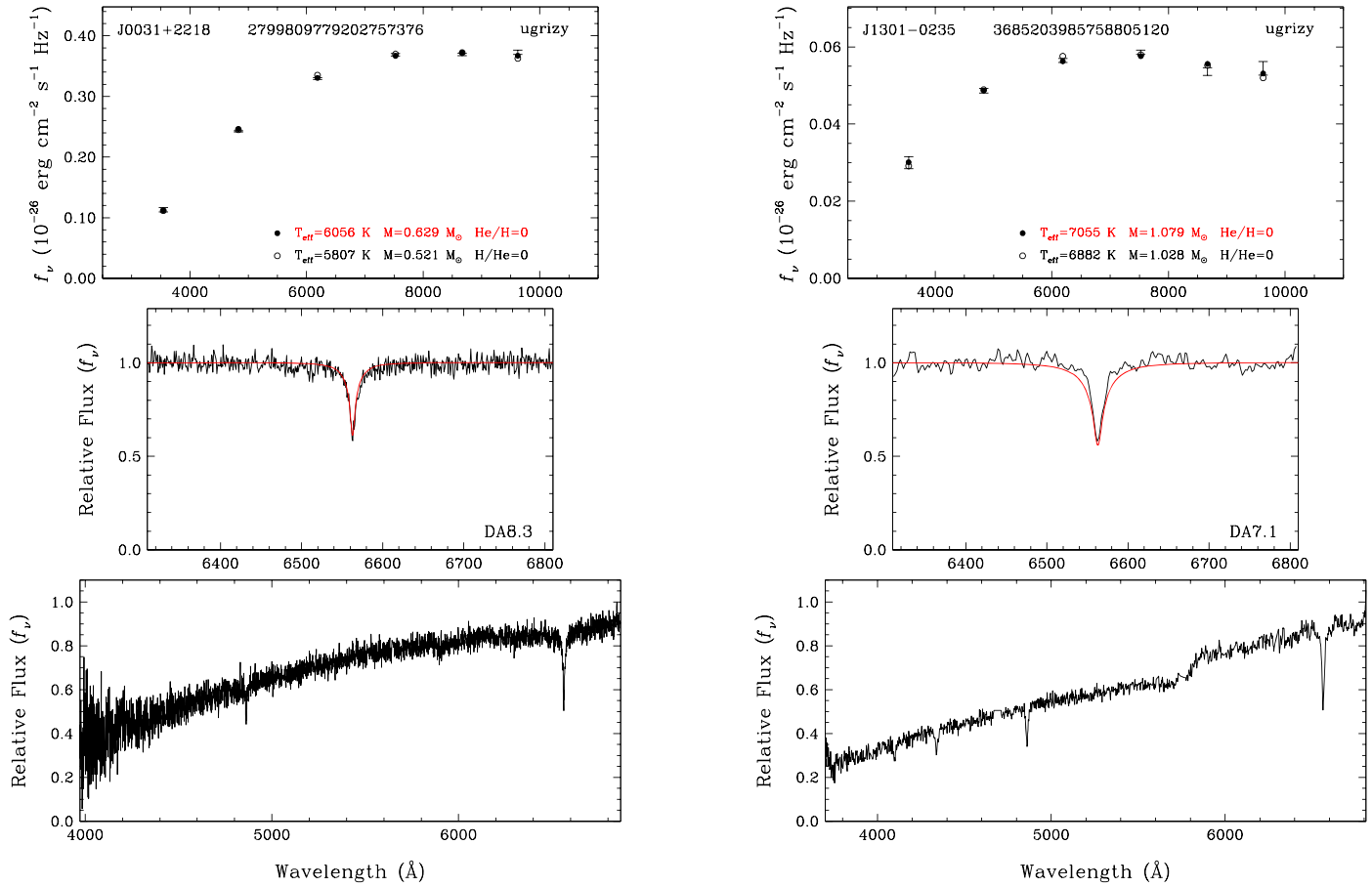

Figure 4. Model fits to new DA white dwarfs observed at the MDM 2.4 m and Gemini South telescopes. The symbols and panels are the same as in Figure 3.

Table 3
Physical Parameters of the DA White Dwarfs

Object	Gaia Source ID	Type	$T_{\rm eff}$ (K)	log$g$ (cm s^{-2})	M ($M_\odot$)
J0000+0132	2738626591386423424	DA	10055 ± 33	7.975 ± 0.009	0.586 ± 0.007
J0003−0111	2449594087142467712	DA	5371 ± 36	8.007 ± 0.043	0.587 ± 0.036
J0004−0340	2447889401738675072	DA	7066 ± 31	7.958 ± 0.009	0.567 ± 0.007
J0006+0755	2746037712074342784	DAH	8610 ± 74	8.183 ± 0.026	0.709 ± 0.023
J0006−0505	2444446482939165824	DA	7157 ± 67	8.156 ± 0.036	0.689 ± 0.031
J0010−2021	2364836107306975872	DA	10049 ± 57	7.919 ± 0.011	0.554 ± 0.009
J0011−0903	2429183303040388992	DA	6203 ± 36	7.931 ± 0.014	0.548 ± 0.012
J0013+0019	2545505281002947200	DA	9507 ± 68	7.985 ± 0.010	0.590 ± 0.009
J0013+3246	2863526233218817024	DA	10309 ± 54	7.889 ± 0.012	0.538 ± 0.009
J0015+1353	2768116146078155648	DA	8439 ± 56	7.936 ± 0.016	0.559 ± 0.012

(This table is available in its entirety in machine-readable form.)

implementation has an accuracy of only ∼0.02 mag according to Tonry et al. (2012).

3.3. Magnetic White Dwarfs

Figure 5 displays our fits to two of the newly identified magnetic DA white dwarfs found in our follow-up survey. J0326+1331 is a relatively warm and massive DA white dwarf with a significant Balmer jump. For magnetic white dwarfs, the Balmer jump is not reproduced well by our nonmagnetic models. Our MDM spectrum of J0326+1331 reveals broad hydrogen lines that are split into multiple components because of the presence of a strong magnetic field. We do not fit for the field strength here, but simply compare the predicted Hα line profile from the photometric fit to the observed spectrum. The observed Hα line profile is weaker than expected, due to the Zeeman splitting, indicating that some of the weak-line objects with noisier spectra may also be magnetic.

J0154+2537 (right panels in Figure 5) is one such system, where at first glance, our MMT spectrum looks noisy. However, a closer look at the Hα region shows that this line is much weaker than expected based on the photometric fit, but it is present and is split into three components by a magnetic field. This figure demonstrates the difficulty of identifying magnetic DA white dwarfs at cooler temperatures, and that some of the DC white dwarfs in our sample may be magnetic

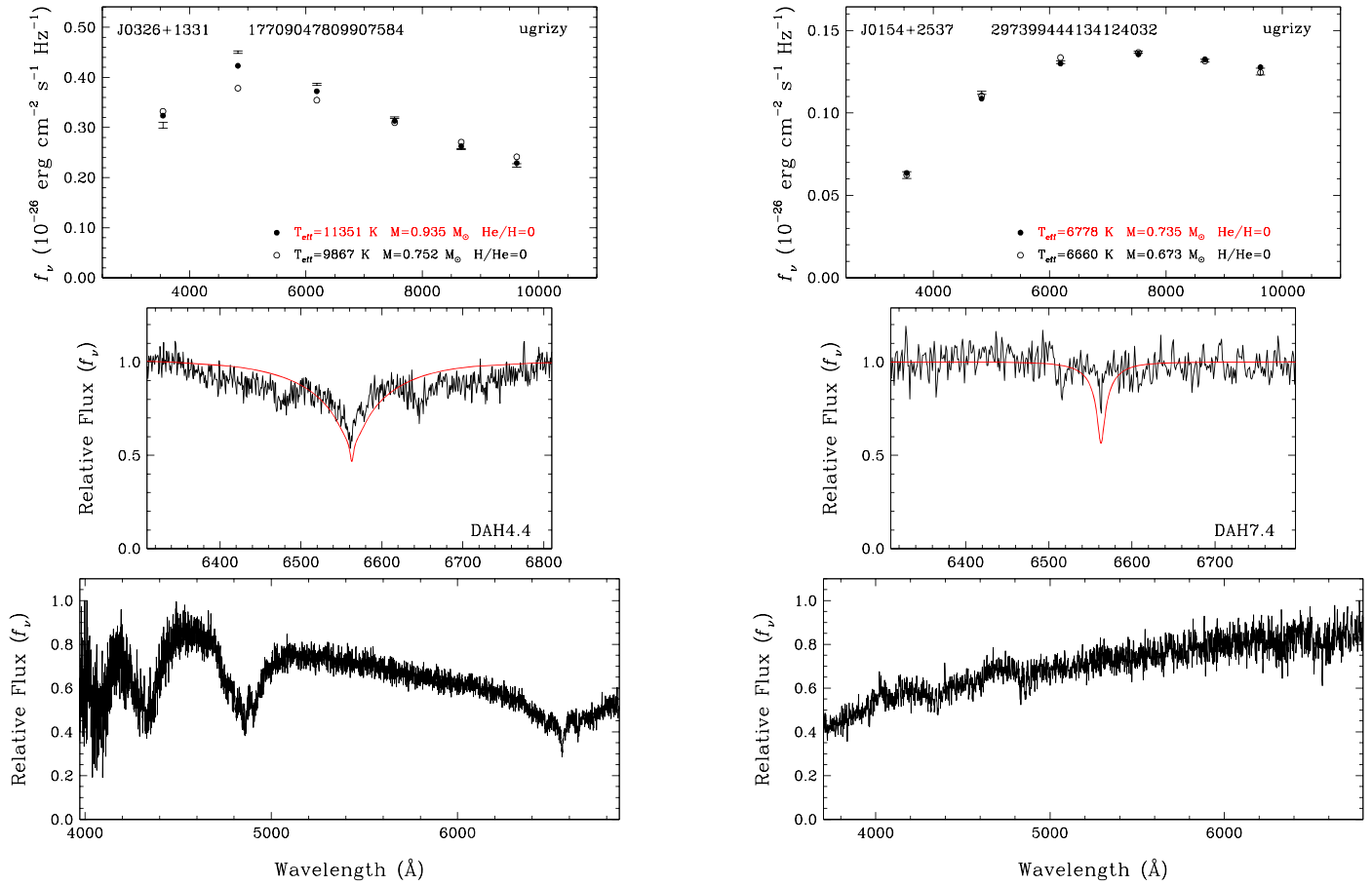

Figure 5. Model fits to two new magnetic DA white dwarfs identified in this work. The symbols and panels are the same as in Figure 3. We do not fit for the magnetic field strength here, but simply overplot the predicted Hα line profile for the best-fitting nonmagnetic, pure hydrogen atmosphere model in the middle panel for each star.

white dwarfs with weak lines that might have been lost in the noise.

Table 3 includes the physical parameters of the magnetic DA white dwarfs, with masses ranging from 0.47 to 1.32 $M_\odot$. The median mass of the magnetic DA white dwarfs in our sample is 0.83 $M_\odot$. This is similar to the average mass, 0.87 $M_\odot$, of the magnetic white dwarfs presented in Kawka (2020). Clearly, the mass distribution for the magnetic white dwarfs is significantly different from that of the normal DA white dwarfs. This is consistent with the idea that magnetic white dwarfs form as a result of merging binaries during common envelope evolution (Briggs et al. 2015).

3.4. He-rich DA White Dwarfs

Ross 640 and L745-46A are some of the best-known examples of DA white dwarfs that have helium-dominated atmospheres. Hydrogen lines in these stars are heavily broadened through van der Waals interactions in helium-dominated atmospheres (Giammichele et al. 2012; Rolland et al. 2018).

Thirteen white dwarfs in our sample show hydrogen lines, but their spectral energy distributions are best explained by a helium-rich atmosphere. Figure 6 shows our model fits to one of these DA(He) white dwarfs. J1646+0308 clearly shows Hα and Hβ. However, the best-fit photometric solution for a pure hydrogen atmosphere has $T_{\rm eff}$ = 12,041 K and $M = 0.86\,M_\odot$. At that temperature, a white dwarf with a pure hydrogen atmosphere would display significantly deeper Balmer lines (top panel) than observed, and the photometry would also show evidence of a significant Balmer jump between the u and g filters, which is not observed. However, the spectral energy distribution and the observed Hα line profile can both be explained by a He-dominated atmosphere with $T_{\rm eff}$ = 10,290 K, $M = 0.617\,M_\odot$, and trace amounts of hydrogen with log H/He = −4.5.

Table 4 presents the best-fit atmospheric parameters for the DA(He) white dwarfs in our sample. The model fits for all 13 are available in the online version of this article. Nine of these are clearly He-dominated DAs, based on the Hα line profiles being inconsistent with a pure hydrogen atmosphere solution. However, for four of these objects, J1611+1322, J1628+1224, J2104+2333, and J2138+2309, our interpretation of a He-dominated atmosphere depends on the quality of the photometry, in particular in the u-band.

These four stars appear as normal DA stars. Using the spectroscopic method, we find that the spectroscopic solution is also consistent with the pure hydrogen photometric solution. However, the spectroscopic method has a degeneracy between a high log$g$ and a high helium content (see Figure 18 in Bergeron et al. 1991). Given the temperature range of 8530–11,060 K for these four stars, the observed Balmer jump between the u and g filters is smaller than expected for pure hydrogen models. The best-fitting mixed atmosphere models

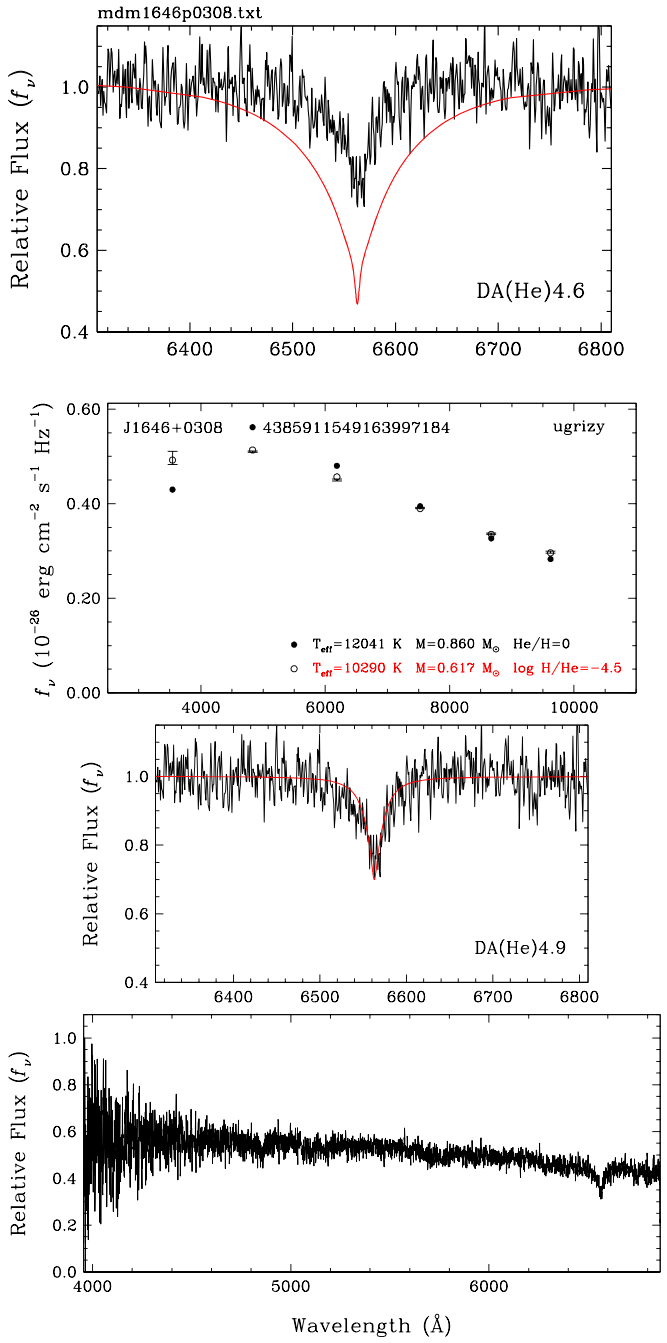

Figure 6. Model fits to the He-rich DA white dwarf J1646+0308. The top panel shows the observed (black) and predicted Hα line (red) for the best-fitting photometric solution with a pure hydrogen atmosphere. The spectral energy distribution clearly favors a He-rich solution (second panel), which provides an excellent match to the Hα line profile (third panel). The bottom panel shows the entire spectral range of our observations, revealing Hα and Hβ lines much weaker than expected for a typical DA white dwarf at these temperatures. All of the He-rich DA white dwarfs are available in the figure set. It has 13 components.

(The complete figure set (13 images) is available.)

have He/H ratios similar to GD 362, which was confirmed to have a helium-dominated atmosphere through high-resolution spectroscopy (Zuckerman et al. 2007). Higher quality u-band photometry or higher resolution optical spectroscopy (for the stars with $T_{\rm eff}$ near 11,000 K) would be useful to confirm the atmospheric compositions for these four targets.

3.5. DC White Dwarfs

He I lines disappear below about 11,000 K, and hydrogen lines disappear below about 5000 K. Hence, the absence of spectral features in DC white dwarfs hotter than 5000 K can be used to rule out a pure H composition and infer a He-dominated atmosphere.

Figure 7 shows our model fits to two of the DC white dwarfs in our sample, where a pure hydrogen atmosphere can be safely ruled out. The photometry cannot distinguish between the pure hydrogen and the helium-dominated solution for J0008−0353 (left panels), as both provide acceptable solutions. However, the best-fitting pure hydrogen atmosphere solution has $T_{\rm eff}$ = 6223 K, which would display a significant Hα line that is not observed in our MMT spectrum. Hence, J0008−0353 clearly has a He-dominated atmosphere. Similarly, the best-fitting pure hydrogen atmosphere model for J0348+8048 (right panels) requires a Hα line that is almost 50% deep compared to the continuum. Such a line is clearly absent in our MDM spectrum, also confirming a He-dominated atmosphere for this white dwarf.

Analyzing the mass distribution of non-DA white dwarfs between 11,000 K and 6000 K, Bergeron et al. (2019) found an almost complete absence of normal-mass non-DA stars based on pure helium atmosphere models, and they concluded that white dwarfs with pure He atmosphere must be extremely rare or nonexistent in this temperature range. More reasonable mass estimates require additional electron donors in the form of hydrogen, carbon, or other metals. In fact, they found that about 25% of the non-DAs in this temperature range are DQ stars contaminated by carbon, and another 25% are DZ stars contaminated by metals, and the rest are DC stars.

Bergeron et al. (2019) and Rolland et al. (2018) revisited the suggestion that convective mixing is responsible for the sudden increase in the number of non-DA white dwarfs below 10,000 K. In this scenario, the relatively small amount of hydrogen in the upper layers is mixed with the underlying helium convection zone, resulting in extremely small hydrogen abundances that, in general, do not produce a visible Hα line.

For the analysis of the DC white dwarfs in our sample, we follow Bergeron et al. (2019) and use mixed hydrogen and helium models where the hydrogen abundance is adjusted as a function of effective temperature. In the temperature range of DB stars ($T_{\rm eff} \geqslant$ 11,000 K), we adopt log H/He = −5, and for cooler DC stars, we gradually increase the hydrogen abundance to log H/He = −3 at 6000 K following the predictions of the convective mixing scenario (Rolland et al. 2018). We assume log H/He = −5 for the He-rich solution of cooler DC stars. Table 5 presents the best-fit model parameters for the newly identified DB and DC white dwarfs in our sample.

For DC white dwarfs below 5000 K, there is no way to tell the composition based on optical spectra as both hydrogen and helium become invisible in their atmospheres. However, pure helium and mixed H/He models result in mass estimates below 0.5 and even 0.4 $M_\odot$ for many of the cool DCs.

Kowalski & Saumon (2006) demonstrated that the far red wing of the Lyman α line dominates the opacity in the blue part of the optical spectra of pure hydrogen atmosphere white dwarfs, and they concluded that most cool DC stars should have pure hydrogen atmospheres. These models provide a much better fit to the $u - g$ colors of the cool DC white dwarfs (see Figures 10 and 11) and provide more reasonable mass estimates of $M > 0.5\,M_\odot$ for the majority of these stars

Table 4
Physical Parameters of the DA White Dwarfs with He-dominated Atmospheres

Object	Gaia Source ID	logH/He	$T_{\rm eff}$ (K)	log$g$ (cm s^{-2})	M ($M_\odot$)
J0048−0124	2530629365419780864	−3.5	9235 ± 100	8.207 ± 0.016	0.708 ± 0.015
J0851+5426	1029968414968983424	−4.0	8782 ± 88	8.275 ± 0.017	0.752 ± 0.016
J1024−0023	3830990156631488128	−4.5	9487 ± 75	8.163 ± 0.019	0.680 ± 0.017
J1159+0007	3891115064506627840	−2.5	8566 ± 44	8.419 ± 0.007	0.849 ± 0.006
J1412+1129	1226246251436497152	−2.0	7360 ± 56	8.225 ± 0.025	0.717 ± 0.022
J1529+1304	1193808772927091712	−4.5	9254 ± 53	8.133 ± 0.011	0.661 ± 0.009
J1611+1322	4458207634145130368	−2.5	8529 ± 50	8.326 ± 0.007	0.786 ± 0.007
J1623+4650	1410031887762012800	−4.0	9206 ± 82	8.177 ± 0.012	0.689 ± 0.011
J1628+1224	4460327252045435648	−1.5	11002 ± 129	7.854 ± 0.018	0.501 ± 0.013
J1646+0308	4385911549163997184	−4.5	10290 ± 68	8.060 ± 0.014	0.617 ± 0.012
J2104+2333	1840865211187303424	−1.0	11059 ± 107	7.932 ± 0.014	0.544 ± 0.011
J2138+2309	1794118516552814336	−1.5	9695 ± 33	7.802 ± 0.007	0.470 ± 0.005
J2301+2323	2842112183412398336	−5.0	9974 ± 52	8.099 ± 0.009	0.641 ± 0.008

Note. The mixed atmosphere interpretation for J1611+1322, J1628+1224, J2104+2333, and J2138+2309 is based on the significance of the Balmer jump inferred from the u-band photometry.

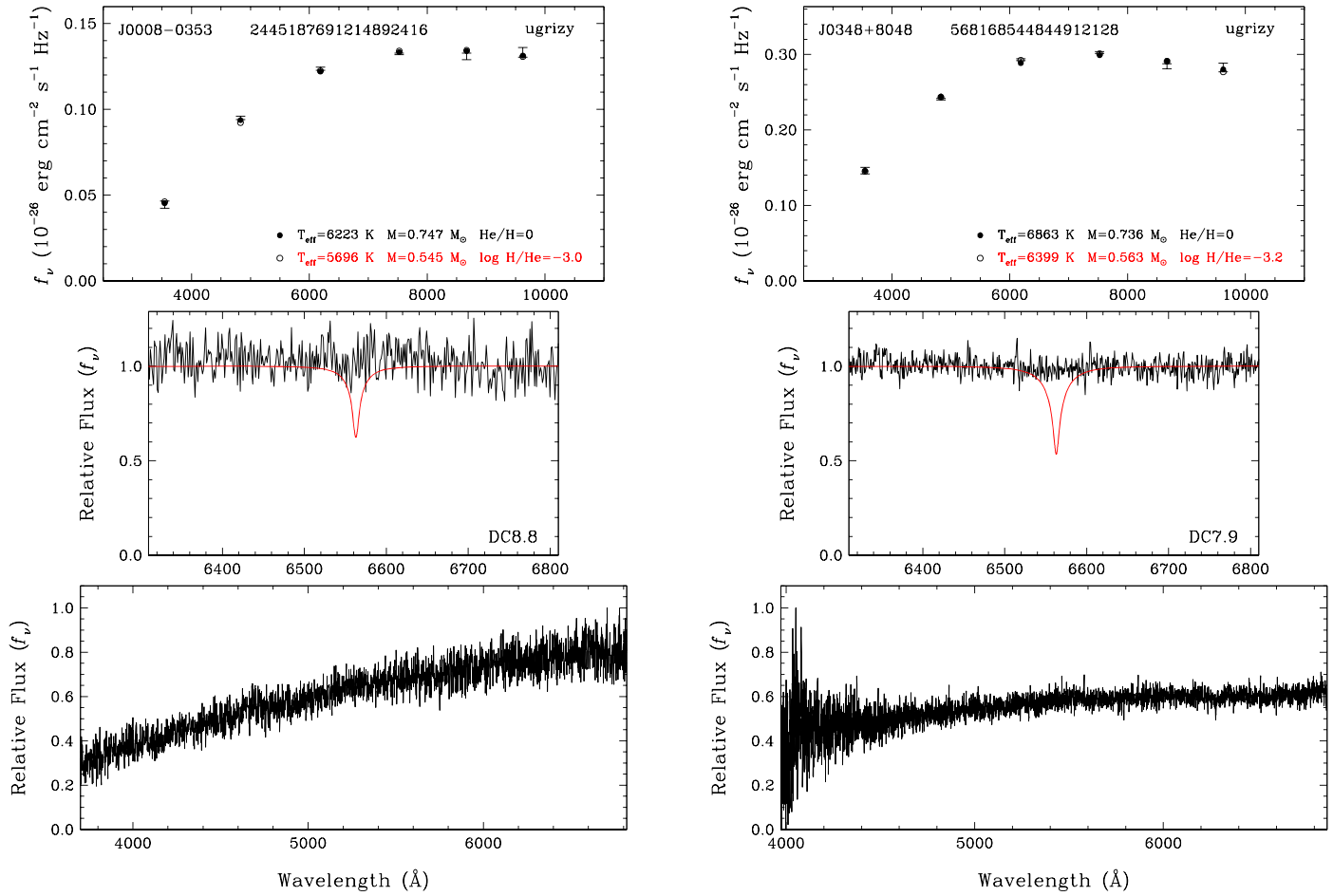

Figure 7. Model fits to two of the DC white dwarfs in our sample. The symbols and panels are the same as in Figure 3. Even though both hydrogen and helium atmosphere solutions match the photometry, pure hydrogen atmosphere models predict significant Hα absorption features that are not observed (middle panels). Hence, these two stars clearly have He-dominated atmospheres. All of the DC white dwarfs are available in the figure set. It has 212 components.
(The complete figure set (212 images) is available.)

(Bergeron et al. 2019). This is why we adopted the pure hydrogen solution for the coolest DCs in our sample.

On the other hand, not all cool white dwarfs have pure hydrogen atmospheres. Blouin et al. (2019) found that ≈25% of the DC white dwarfs cooler than 5000 K have helium-rich atmospheres. There are also DZ white dwarfs with clearly helium-rich atmospheres in the same temperature range. The atmospheric composition of each of the cool DCs should be

Table 5
Physical Parameters of the DB and DC White Dwarfs

Object	Gaia Source ID	Type	logH/He	$T_{\rm eff}$ (K)	log$g$ (cm s^{-2})	M ($M_\odot$)
J0001+3237	2874216647336589568	DC	−5.0	5447 ± 54	7.771 ± 0.045	0.441 ± 0.033
J0005+3451	2876705018245556480	DC	−4.6	10138 ± 73	7.965 ± 0.015	0.561 ± 0.012
J0008−0353	2445187691214892416	DC	−5.0	5714 ± 52	7.953 ± 0.041	0.543 ± 0.034
J0011+2824	2859908324567852416	DC	−3.8	8243 ± 91	7.872 ± 0.021	0.503 ± 0.017
J0011−0827	2429268309033277184	DC	−4.0	8616 ± 94	8.130 ± 0.028	0.658 ± 0.025
J0014−0758	2429392661221943040	DC	−5.0	5585 ± 51	8.017 ± 0.048	0.581 ± 0.041
J0019−1114	2424913628807069056	DC	−3.8	8187 ± 64	8.093 ± 0.025	0.633 ± 0.022
J0021+3827	378856389416637056	DC	−5.0	11332 ± 86	8.057 ± 0.011	0.617 ± 0.010
J0038+3409	364978005758397952	DC	−4.2	9191 ± 58	7.923 ± 0.018	0.534 ± 0.014
J0049+1727	2782037303315690752	DC	−3.0	5790 ± 66	7.961 ± 0.057	0.548 ± 0.047

(This table is available in its entirety in machine-readable form.)

constrained based on a detailed analysis of each object, which is outside the scope of this paper.

There are several DC white dwarfs in our sample that display significant absorption in the Pan-STARRS z and y bands. These are the so-called IR-faint or ultracool white dwarfs that display collision-induced absorption (CIA) from molecular hydrogen. We discuss these further in Section 4.3.

3.6. DQ White Dwarfs

We identify seven new DQ white dwarfs in our survey. We rely on the photometric technique to determine the best-fit $T_{\rm eff}$ and log$g$ for these stars and use the neutral C I lines or the C_2 Swan bands to fit for C/He. Given the abundances derived from the spectroscopic fit, we repeat our photometric and spectroscopic fits until a consistent solution is found. Figure 8 shows our model fits to two of these stars. The top and middle panels show our photometric and spectroscopic fits, respectively. The DQ models presented in Blouin et al. (2019) provide an excellent match to both the photometry and spectroscopy data for these stars.

Table 6 presents the best-fit model parameters for all seven newly identified DQ white dwarfs in our sample. Six of these are cooler than 8000 K and display strong C_2 Swan bands in their spectra. The remaining object, J0104+4650, is significantly hotter and has a relatively noisy MDM spectrum that displays weaker lines. A higher signal-to-noise ratio spectrum would be helpful in confirming the nature of this system and constraining its carbon abundance. The best-fit parameters for J0104+4650, $T_{\rm eff} = 11{,}257 \pm 166$ K, $M = 0.997 \pm 0.016\,M_\odot$, and logC/He $= -3.21$, place it in the second and more massive DQ white dwarf sequence as discussed in Blouin & Dufour (2019), Koester & Kepler (2019), and Coutu et al. (2019).

3.7. DZ White Dwarfs

There are 27 newly identified DZ white dwarfs in our sample that display Ca H and K absorption lines. We rely on the photometric technique to determine the temperature and surface gravity for these stars, and we fit the blue portion of the spectrum, including the Ca II H and K doublet and the Ca I resonance line, to find Ca/He. We use the red portion of the spectrum to constrain the H/He abundance ratio. The abundance ratios of the other heavy elements are scaled to the abundance of Ca to match the abundance ratios of CI chondrites. Figure 9 shows our model fits to two of these stars. The top and middle panels for each star show our photometric and spectroscopic fits, respectively. The bottom panels show the entire spectral range of the data.

J0422+0038 (left panels) is a cool DZ white dwarf that shows only Ca absorption features. The absence of a Hα absorption feature constrains the H/He ratio in this star, and our model fits provide an excellent match to both the optical spectra and the photometry of this star. The best-fit model has logH/He $= -3$ and logCa/He $= -9.34$.

J1733+3013 (right panels) is a DZ with both Ca and Mg lines. Our FAST spectrum does not cover Hα, but Hβ is clearly absent in this star. Our best-fit model with logCa/He $= -7.85$ reproduces most of the observed Ca absorption lines relatively well in the blue. The model fits for the rest of the DZ white dwarfs are presented in the online version of this article, and the best-fit parameters are presented in Table 7. The Ca abundances for these stars range from logCa/He $= -11.3$ to -7.9.

4. Discussion

4.1. The 100 pc White Dwarf Sample in the SDSS Footprint

With the addition of 711 new spectra from our spectroscopic survey, we have spectral types for 2361 of the 4016 white dwarfs in the 100 pc white dwarf sample in the SDSS footprint. We classify 1539 (or 65%) as DA, including 85 magnetic white dwarfs, 13 DA(He) stars with He-dominated atmospheres, 1 DAB white dwarf (GD 323), 5 DA + M dwarf systems, and 9 with likely but uncertain DA classification. We also identify 53 DB/DBA, 555 (or 24%) DC, 97 DQ, 115 DZ, 1 cataclysmic variable (ASASSN-14dx), and 1 dwarf nova (GD 552).

Figure 10 shows the distribution of DA and non-DA stars in color–magnitude diagrams based on Gaia (left panel) and SDSS u and Pan-STARRS g photometry (right panel). The solid, dashed, and dotted lines show the cooling sequences for 0.6 $M_\odot$ white dwarfs with pure hydrogen, pure helium, and mixed atmosphere models with logH/He $= -5$, respectively. The bifurcation in $u - g$ colors is easily explained by the Balmer jump in white dwarfs with a pure hydrogen atmosphere. The Balmer jump suppresses the ultraviolet fluxes of

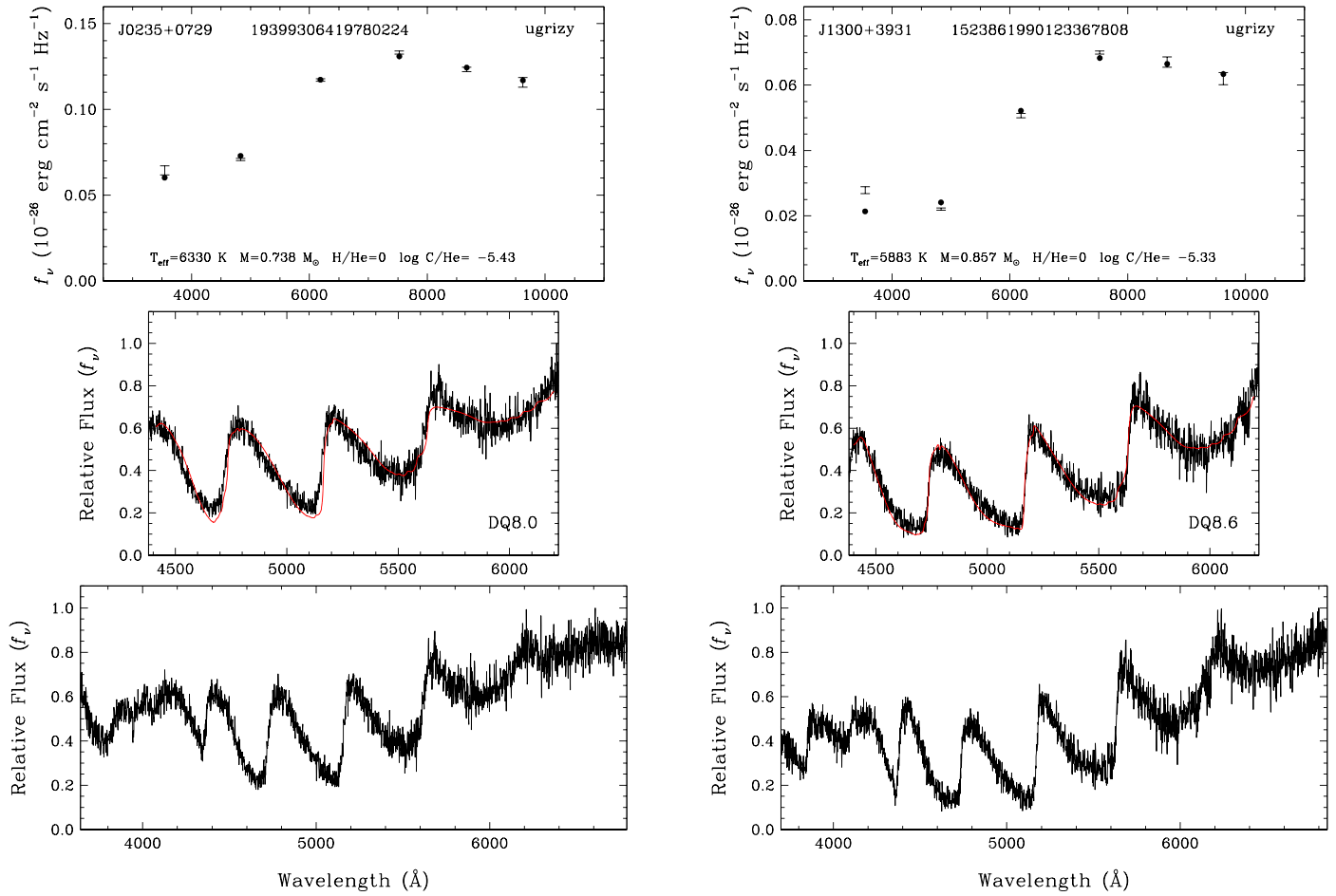

Figure 8. Model fits to two DQ white dwarfs observed at the MMT. The top and middle panels show the photometric and spectroscopic model fits, respectively. The bottom panels display the entire spectral range of the observations. The atmospheric models provide an excellent match to both photometry and spectroscopy for these two stars. All of the DQ white dwarfs are available in the figure set. It has seven components.

(The complete figure set (7 images) is available.)

Table 6
Physical Parameters of the DQ White Dwarfs

Object	Gaia Source ID	logC/He	$T_{\rm eff}$ (K)	log$g$ (cm s^{-2})	M ($M_\odot$)
J0104+4650	401215160231429120	−3.21	11257 ± 166	8.646 ± 0.020	0.997 ± 0.016
J0235+0729	19399306419780224	−5.43	6330 ± 19	8.251 ± 0.025	0.733 ± 0.023
J0441−0551	3200232157189930880	−5.72	7619 ± 49	7.957 ± 0.013	0.550 ± 0.011
J0705−1703	2935415125246460032	−5.42	6116 ± 25	8.156 ± 0.024	0.670 ± 0.022
J1241+2614	3961323069532233984	−6.94	5794 ± 17	7.946 ± 0.027	0.539 ± 0.022
J1300+3931	1523861990123367808	−5.33	5883 ± 22	8.429 ± 0.035	0.852 ± 0.032
J1706−1238	4140966708116861440	−6.83	6113 ± 42	7.943 ± 0.045	0.538 ± 0.036

these stars compared to their hydrogen-poor counterparts, resulting in redder $u - g$ colors.

The split in the Gaia sequence is also explained by the presence of hydrogen (or other electron donors), but in this case it is the additional opacity from trace amounts of hydrogen in helium-dominated white dwarfs that affects their colors (Bergeron et al. 2019). The logH/He $= -5$ mixed atmosphere model sequence, for example, goes through the bulk of the DC white dwarfs in the Gaia color–magnitude diagram, except the coolest ones. Regardless of the reason (additional hydrogen or other electron donors), the differences in atmospheric composition can clearly explain the bifurcation seen in these color–magnitude diagrams.

Figure 11 shows a color–color diagram of our white dwarf sample based on the SDSS u and Pan-STARRS g, r filters. DA and DB/DC white dwarfs form relatively tight color sequences in this diagram, with the main distinction between them being the Balmer jump visible in the $u - g$ color for DA white

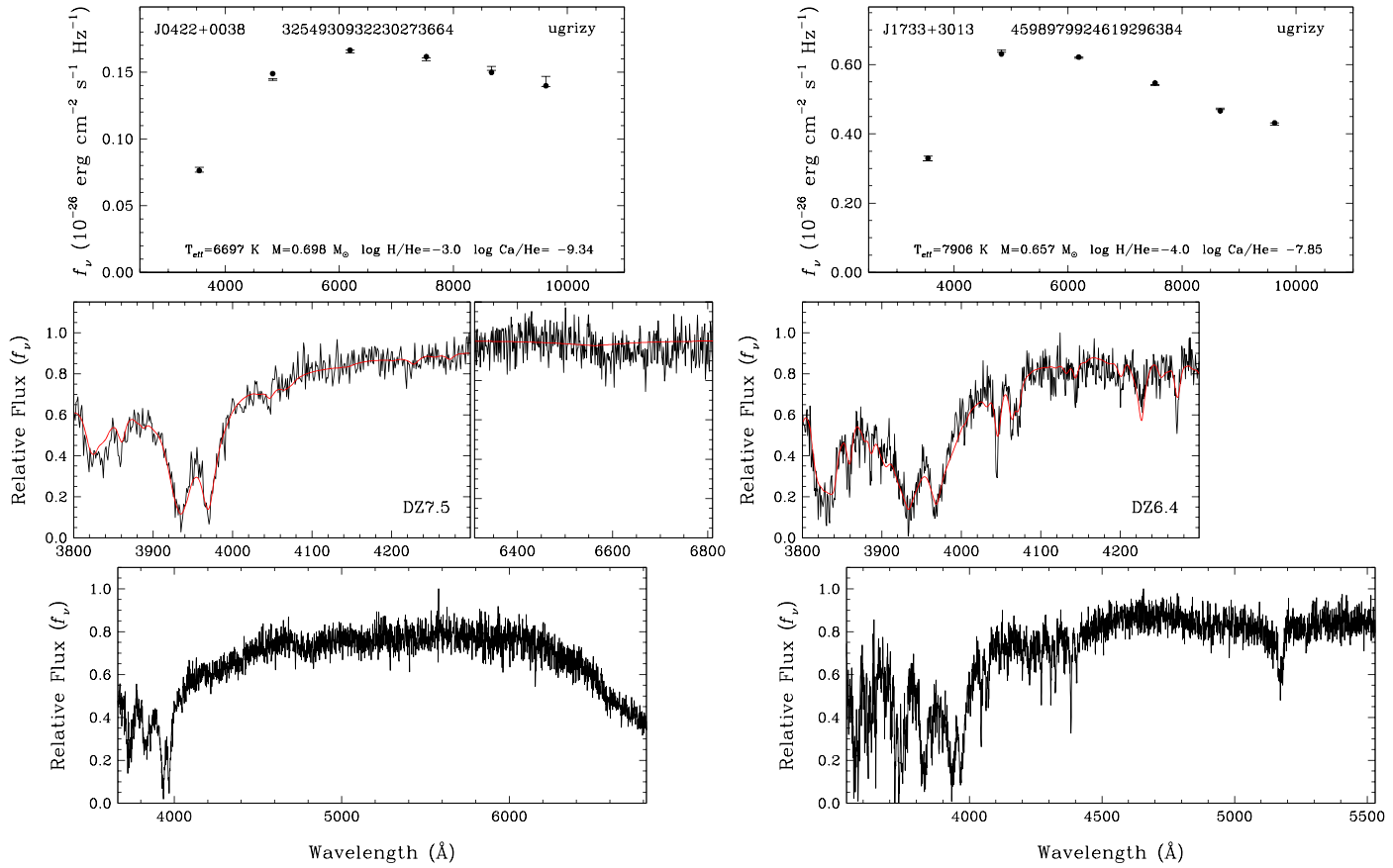

Figure 9. Model fits to two DZ white dwarfs observed at the MMT and FAST. The top and middle panels show the photometric and spectroscopic model fits, respectively. The bottom panels display the entire spectral range of the observations. The atmospheric models provide an excellent match to both photometry and spectroscopy for these two stars. All of the DZ white dwarfs are available in the figure set. It has 27 components.

(The complete figure set (27 images) is available.)

dwarfs. On the other hand, the majority of the DQ (green) and DZ (magenta) white dwarfs appear as outliers with respect to the DA and DB/DC sequences.

DZ white dwarfs suffer from metal absorption features mostly in the ultraviolet, which result in redder $u - g$ colors compared to DC stars, whereas the Swan bands in DQ white dwarfs are strongest in the g filter, resulting in bluer $u - g$ or redder $g - r$ colors compared to the DC white dwarfs. Hence, follow-up spectroscopy of the outliers in similar color–color diagrams may provide an efficient method to identify additional DQ and DZ white dwarfs in the solar neighborhood.

A striking feature visible in Figures 10 and 11 is that the cooling sequences for 0.6 $M_\odot$ pure helium and mixed H/He atmosphere white dwarfs fail to match the colors of the bulk of the cool DC white dwarfs with $u - g > 0.8$ mag, or $T_{\rm eff} <$ 6000 K. Hence, a photometric analysis based on helium-rich models produces mass estimates that are too low (see Figure 12 in Bergeron et al. 2019). On the other hand, the pure hydrogen atmosphere models including the red wing of the Lyman α line (Kowalski & Saumon 2006) provide a much better fit to the $u - g$ colors of the cool DC white dwarfs in Figures 10 and 11 and provide more normal mass estimates, justifying our use of pure hydrogen model fits for the coolest ($T_{\rm eff} < 5000$ K) DCs in our sample.

A caveat in our analysis is that some of the cool DCs likely have helium-dominated atmospheres. Comparing the pure hydrogen, pure helium, and mixed H/He atmosphere solutions for each star, Blouin et al. (2019) found the fraction of helium-rich DCs to be around 25%. Based on the $u - g$ colors, the fraction of DC stars that have helium-rich atmospheres appears to be small in our sample. However, a detailed model atmosphere analysis of individual DC white dwarfs is required for reliable constraints on their atmospheric parameters.

In the following sections, we present the DA white dwarf mass distribution, and we then discuss the properties of the DC white dwarfs, specifically the so-called IR-faint white dwarfs in our sample.

4.2. DA Mass Distribution

Figure 12 shows a color–magnitude diagram of all spectroscopically confirmed DA white dwarfs in our sample. The DA white dwarf sequence ends at an absolute magnitude of $M_G \approx 15$, which corresponds to $T_{\rm eff} = 5000$ K for 0.6 $M_\odot$ white dwarfs. Hα disappears below this temperature. Excluding the DA white dwarfs with weak lines, mixed atmospheres, for example, DA(He) stars, uncertain spectral types, or M dwarf companions, we have 1508 spectroscopically confirmed DA white dwarfs in our sample that are best fit by pure hydrogen atmosphere models. Most of these DA white dwarfs form a tight sequence around $M = 0.6\,M_\odot$, but a significant contribution from fainter and more massive white dwarfs, many of which are on the the crystallization sequence (also referred

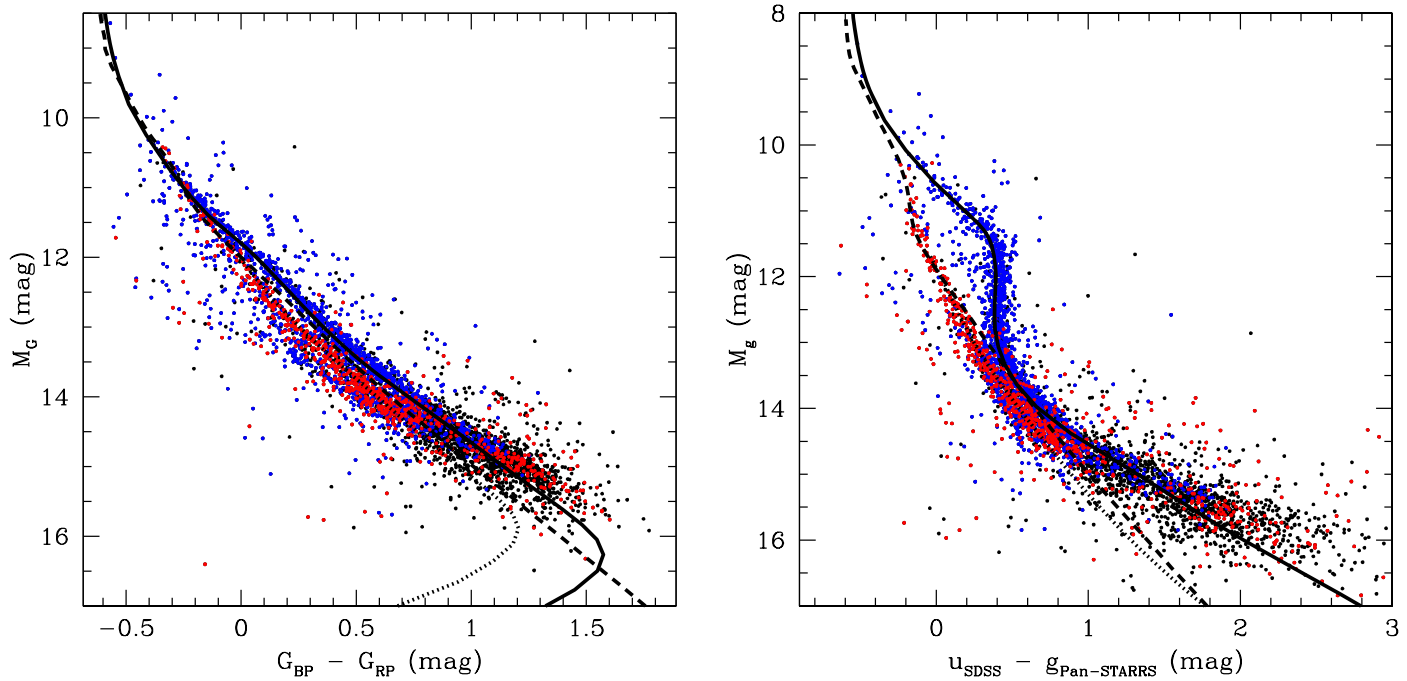

Figure 10. Gaia (left) and SDSS + Pan-STARRS (right) color–magnitude diagrams of the 100 pc white dwarf sample in the SDSS footprint. Blue and red points mark the spectroscopically confirmed DA and non-DA white dwarfs, respectively. The remaining objects with no follow-up spectroscopy are shown as black dots. The bifurcation between the DA and non-DA white dwarfs is clearly observed in these diagrams. The solid, dashed, and dotted lines show the cooling sequences for 0.6 $M_\odot$ white dwarfs with pure hydrogen, pure helium, and mixed atmosphere models with logH/He = −5, respectively.

Table 7
Physical Parameters of the DZ White Dwarfs

Object	Gaia Source ID	logCa/He	logH/He	$T_{\rm eff}$ (K)	log$g$ (cm s^{-2})	M ($M_\odot$)
J0115+4733	401529105161219968	−10.88	−3	6436 ± 63	8.220 ± 0.054	0.712 ± 0.050
J0141+2257	290602027028411136	−7.93	−3	7562 ± 33	8.044 ± 0.015	0.602 ± 0.013
J0333+0656	3276355500412926336	−9.62	−4	7037 ± 73	8.149 ± 0.041	0.667 ± 0.037
J0416+2947	165677710612522752	−9.72	−4	6864 ± 59	8.091 ± 0.023	0.630 ± 0.021
J0422+0038	3254930932230273664	−9.34	−3	6696 ± 39	8.211 ± 0.024	0.707 ± 0.022
J0425+2834	152931141027253888	−10.40	−2	5988 ± 31	8.145 ± 0.020	0.662 ± 0.018
J0445+0050	3230171064244273024	−10.14	−4	6071 ± 35	8.110 ± 0.027	0.640 ± 0.024
J0447+0106	3231702860037325824	−10.95	−2	6164 ± 43	8.188 ± 0.017	0.691 ± 0.016
J0654+3938	950361883331847424	−9.58	−4	9435 ± 68	7.961 ± 0.010	0.556 ± 0.008
J0703−1656	2935446392608812032	−11.27	−4	7387 ± 68	8.080 ± 0.021	0.624 ± 0.018
J0717+3630	898002379406954752	−9.10	−4	7133 ± 61	8.101 ± 0.029	0.637 ± 0.025
J0726+2216	866081701427025536	−8.78	−4	6957 ± 40	7.991 ± 0.019	0.569 ± 0.016
J0800−0840	3039671225803688320	−9.93	−4	6965 ± 60	8.135 ± 0.019	0.658 ± 0.017
J0805+6624	1095169656358227456	−10.94	−4	6482 ± 80	8.066 ± 0.031	0.613 ± 0.027
J0902+6503	1044511002434919936	−10.34	−4	6385 ± 54	8.121 ± 0.022	0.648 ± 0.019
J0912+0808	590183142750379136	−10.47	−4	6338 ± 47	8.056 ± 0.019	0.607 ± 0.017
J0928+1937	634307433430523648	−10.43	−4	6072 ± 34	8.050 ± 0.028	0.602 ± 0.025
J1027+5019	847272257226467840	−10.71	−2	5742 ± 48	8.135 ± 0.034	0.656 ± 0.031
J1114+6546	1056003918305358592	−10.40	−4	5915 ± 40	8.196 ± 0.018	0.696 ± 0.016
J1137+2005	3978988652273088128	−11.17	−3	6214 ± 49	8.201 ± 0.043	0.700 ± 0.039
J1502+4933	1592242645479324288	−9.79	−4	6541 ± 46	8.109 ± 0.021	0.641 ± 0.018
J1552−0219	4403059253334693248	−9.53	−4	7666 ± 59	8.018 ± 0.021	0.586 ± 0.018
J1733+3013	4598979924619296384	−7.85	−4	7908 ± 38	8.146 ± 0.008	0.667 ± 0.007
J1757+1021	4494877446445481472	−8.28	−4	8358 ± 46	8.101 ± 0.008	0.639 ± 0.007
J1759+0349	4469700519955285760	−9.92	−4	11170 ± 86	7.774 ± 0.014	0.460 ± 0.010
J2025+2839	1860318973495642240	−9.03	−4	11197 ± 100	7.913 ± 0.013	0.533 ± 0.010
J2058+1657	1764481588648685440	−8.38	−1	6284 ± 27	8.312 ± 0.023	0.774 ± 0.022

to as the Q-branch, Gaia Collaboration et al. 2018; Tremblay et al. 2019), is also clearly visible.

Figure 13 shows the mass distribution of our DA white dwarf sample. Since our spectroscopic completeness falls significantly beyond 6000 K, we limit our mass distribution to 1337 stars with $T_{\rm eff} \geqslant 6000$ K. We estimate the uncertainties in each mass bin based on a Monte Carlo analysis, where we replace the mass of each white dwarf M with $M + g\ \delta M$, where $\delta\ M$ is the error in

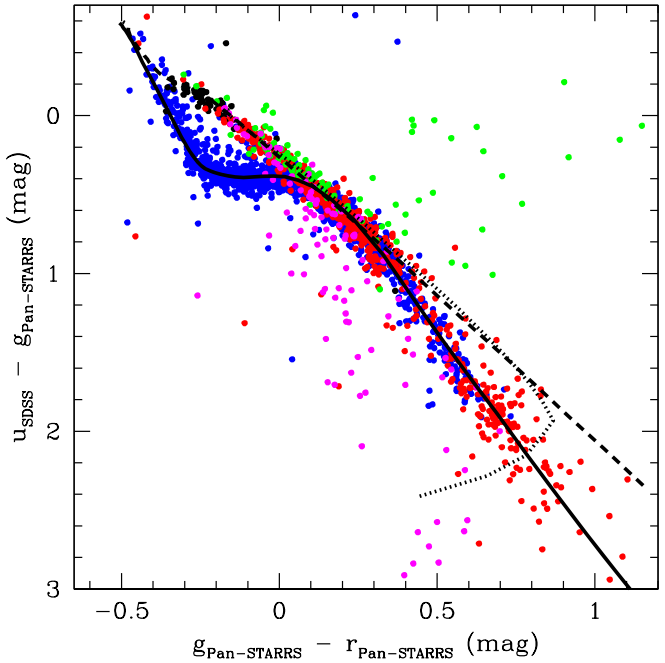

Figure 11. Color–color diagram of the DA (blue), DB (black), DC (red), DQ (green), and DZ (magenta) white dwarfs in the 100 pc sample and the SDSS footprint. The model sequences are the same as in Figure 10. DA and DB/DC white dwarfs form relatively tight sequences in this diagram, whereas many of the DQ and DZ stars show up as outliers.

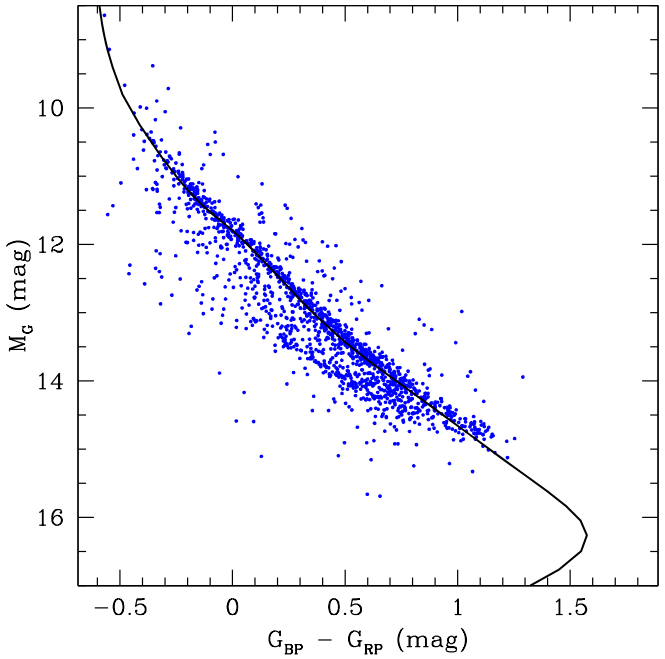

Figure 12. Color–magnitude diagram of the spectroscopically confirmed DA white dwarfs in the 100 pc sample and the SDSS footprint. The solid line shows the cooling sequence for a 0.6 $M_\odot$ pure hydrogen atmosphere white dwarf.

mass, and g is a Gaussian deviate with zero mean and unit variance. For each of 1000 sets of modified masses for the entire sample, we calculate the mass distribution, and we take the range that encompasses 68% of the probability distribution function as the 1σ uncertainty for each mass bin.

Remarkably, the mass distribution has an extremely narrow peak and a broad shoulder. Fitting two Gaussians to the

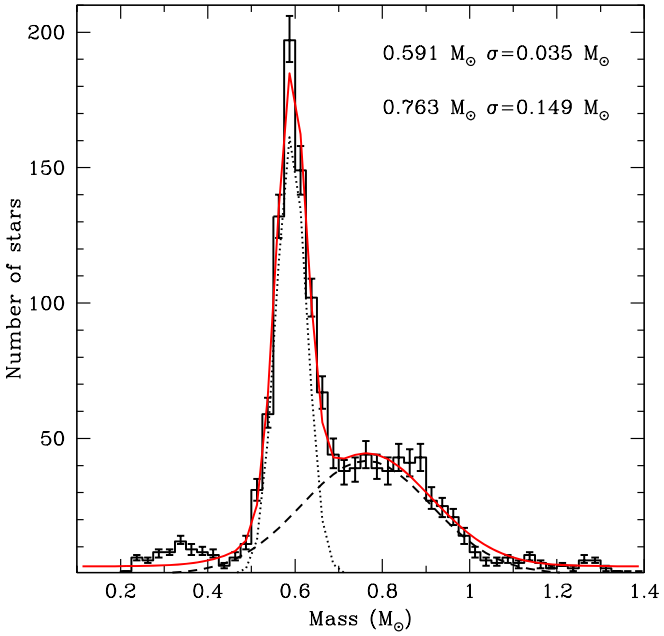

Figure 13. White dwarf mass distribution (black solid histogram) based on 1337 spectroscopically confirmed DA white dwarfs hotter than 6000 K in the 100 pc sample and the SDSS footprint. Dotted and dashed lines show the best-fitting Gaussians to the main peak and the broad shoulder, and the red line shows the composite of the two.

observed distribution, we find that the mean peak is centered at 0.59 $M_\odot$ with a 1σ spread of only 0.035 $M_\odot$, whereas the contribution from massive white dwarfs is best fit with a Gaussian at 0.76 $M_\odot$ and a 1σ spread of 0.15 $M_\odot$. There is also a low-mass peak around 0.35 $M_\odot$ in the mass distribution, but it is smaller than previously observed in magnitude-limited samples like the PG survey (Liebert et al. 2005). This is not surprising as low-mass white dwarfs are overrepresented in magnitude-limited surveys, due to their larger radii and luminosities. A caveat here is that our mass estimates for low-mass white dwarfs may be erroneous since they were based on the assumption of a single star, and low-mass white dwarfs are usually found in binary systems (Marsh et al. 1995; Kilic et al. 2020). Hence, further observations would be useful for constraining the binary nature of these systems and the mass distribution below 0.5 $M_\odot$.

Figure 14 compares the DA mass distributions for $T_{\rm eff} \geqslant 6000$ K (left panel) and a more restrictive $T_{\rm eff} \geqslant 10{,}000$ K (right panel) sample of stars against the predictions from a 10 Gyr old disk population with a constant star formation rate (SFR, solid line) and a Gaia magnitude limit of $G = 20$. We use a Salpeter mass function (Salpeter 1955) and assume solar metallicity and that the stars evolve in isolation. We use the main-sequence + giant-branch lifetimes from Hurley et al. (2000) to decide if a star evolves into a white dwarf within 10 Gyr, and if so, to estimate its cooling age.

We calculate the final white dwarf masses based on the latest MIST-based piece-wise IFMR from Cummings et al. (2018), and we use the evolutionary models[6] similar to those described in Fontaine et al. (2001) with (50/50) C/O-core compositions, $q({\rm He}) \equiv M_{\rm He}/M_\star = 10^{-2}$, and $q({\rm H}) = 10^{-4}$, to estimate their temperatures. Just like in the observed samples, we only include white dwarfs with $T_{\rm eff} \geqslant 6000$ K (left panel) or

[6] See http://www.astro.umontreal.ca/~bergeron/CoolingModels.

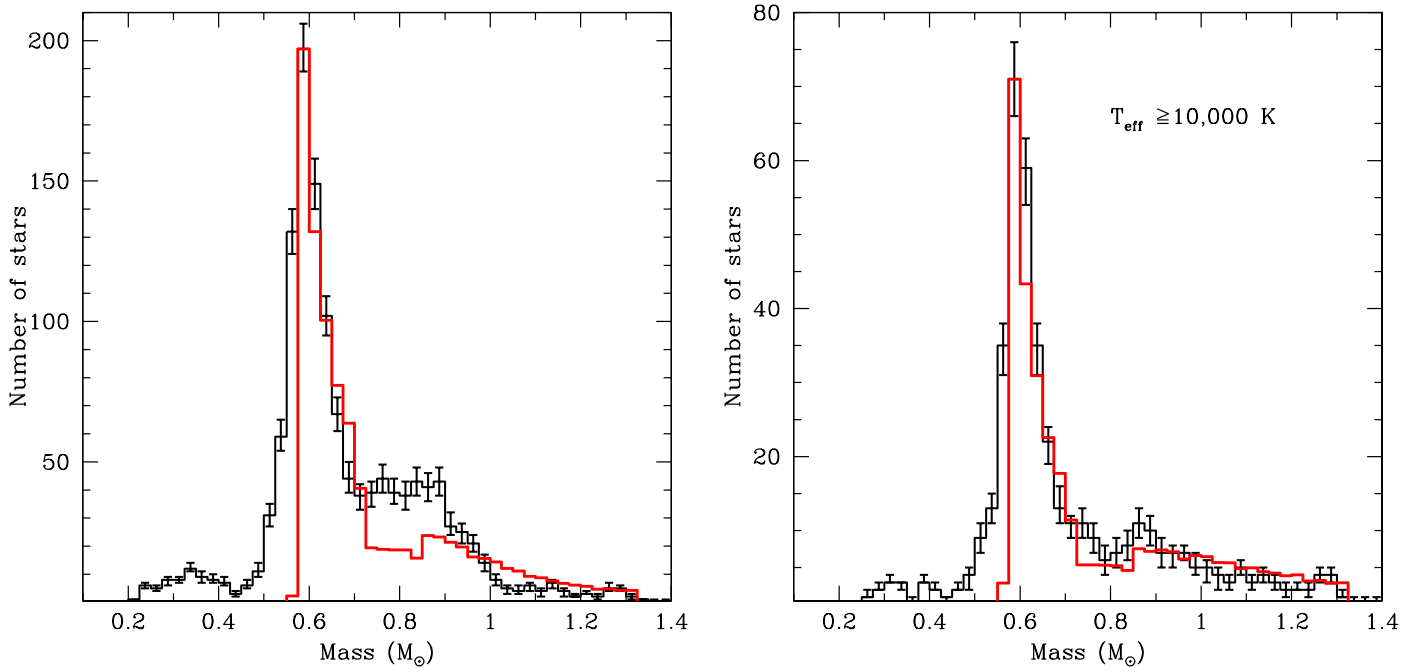

Figure 14. Left panel: the DA white dwarf mass distribution (black histogram) compared to the predicted mass distribution for a 10 Gyr old disk population that evolved in isolation (red line). Right panel: the same as in the left panel, but for a more restrictive sample of white dwarfs with $T_{\rm eff} \geqslant 10,000$ K.

10,000 K (right panel) in these simulations. We normalize the disk model to match the peak of the observed mass distribution at 0.59 $M_\odot$. Our simulations fail to account for the relatively large numbers of low-mass ($M < 0.5\,M_\odot$) white dwarfs. This is not surprising, as the majority of these low-mass white dwarfs are likely in binary white dwarf systems (Marsh et al. 1995), which are excluded from our synthetic populations.

This figure reveals remarkable differences between the mass distributions for the hot DAs and the overall population. The mass distribution for the hot DAs (right panel) shows a roughly linear decline in the number of massive white dwarfs beyond 0.7 $M_\odot$, and the 10 Gyr old disk model of single stars with constant star formation provides an excellent match to this mass distribution. Note that we simply scaled the model predictions to match the peak of the observed mass distribution, so the excellent match between the observations and the predictions demonstrates that our choices of a Salpeter IMF, a constant SFR, the IFMR, and the white dwarf cooling models are appropriate for simulating white dwarf populations in the solar neighborhood. At 10,000 K, only white dwarfs more massive than 1 $M_\odot$ would have crystallized. Hence, the uncertainties in the cooling models due to crystallization and its associated effects (see below) are mostly avoided for hot white dwarfs.

Even though both the hot DA and the overall DA mass distributions peak at 0.59 $M_\odot$, the latter (left panel) is significantly different: it shows a nearly constant number of massive white dwarfs between 0.7 and 0.9 $M_\odot$, and then a sudden decrease to nearly zero at 1 $M_\odot$ and beyond. The synthetic populations fail to match this distribution. This figure demonstrates that for cool white dwarfs there is a mechanism that leads to a pile-up of massive white dwarfs with $M \sim 0.8\,M_\odot$ and a sudden disappearance of more massive white dwarfs.

4.2.1. Effects of Mergers on the Mass Distribution

Liebert et al. (2005) interpreted the excess of massive white dwarfs in the Palomar–Green Survey of DA white dwarfs as evidence of binary evolution. Toonen et al. (2017) performed binary population synthesis calculations to show that up to 23% of the white dwarfs in the solar neighborhood might have descended from binary mergers during (post-)main-sequence evolution. Recently, Temmink et al. (2020) found that binary mergers can account for 10%–30% of all single white dwarfs. However, they found that these mergers should not significantly alter the shape of the white dwarf mass distribution.

Now that we have a precise mass distribution based on 1337 spectroscopically confirmed white dwarfs with $T_{\rm eff} \geqslant 6000$ K in a volume-limited sample, we can directly compare the predictions from the binary population synthesis calculations to see if mergers can explain the overabundance of massive white dwarfs in our sample.

We use the binary-star evolution (BSE) algorithm of Hurley et al. (2002) to track the evolution of 10^5 main-sequence binaries with primary masses randomly drawn between 0.8 and 8 $M_\odot$ from a Salpeter mass function and the secondary masses drawn from a uniform mass ratio distribution between 0 and 1. We assume a constant star formation rate and track the evolution of these systems over 10 Gyr. We perform simulations with two different period distributions: lognormal and flat (Toonen et al. 2017). We use the evolutionary times from BSE to estimate the cooling age of each single white dwarf that formed through mergers and estimate its current temperature based on the white dwarf cooling models.

Figure 15 in the top panel shows the predicted mass distribution for single white dwarfs that form as a result of mergers. The results from the lognormal and flat period distributions are shown as solid and dotted lines, respectively. The overall shapes of the predicted mass distributions are

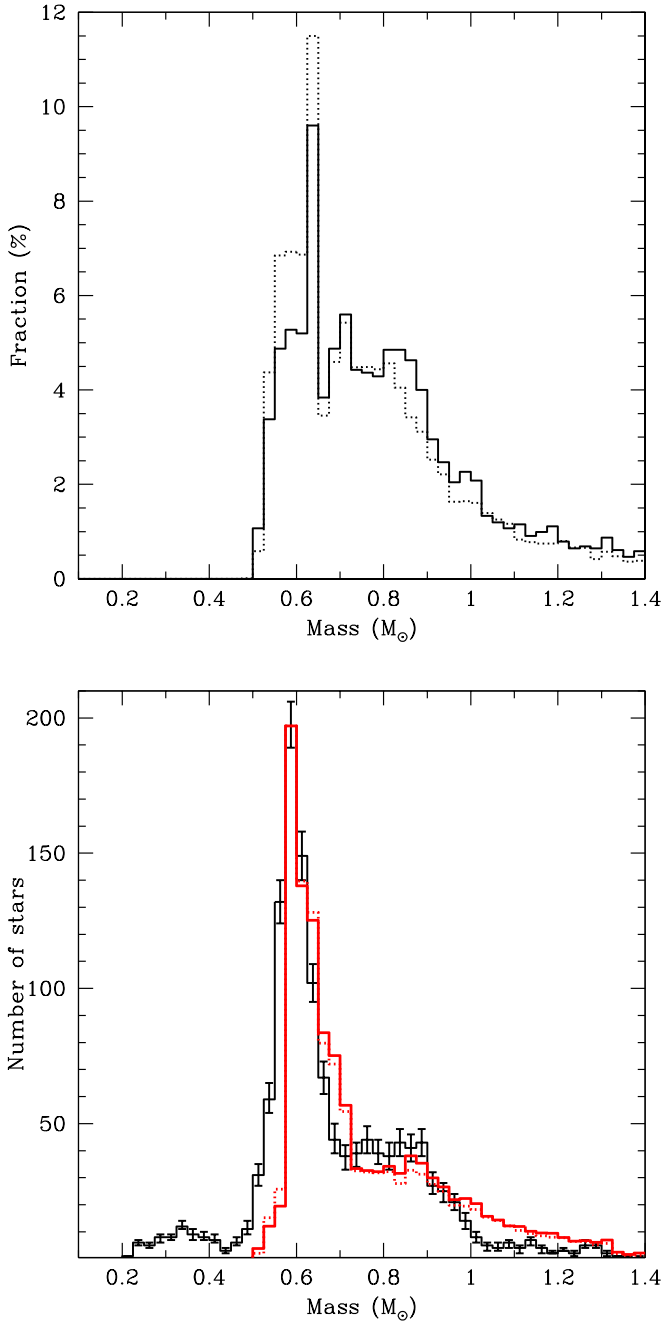

Figure 15. Top panel: predicted mass distribution for single white dwarfs that form through mergers during their main-sequence or post-main-sequence evolution. The solid and dotted lines show the results assuming an initial lognormal and flat period distribution for the progenitor main-sequence stars, respectively. Bottom panel: the DA white dwarf mass distribution (black histogram) compared to the predicted mass distribution with 30% contribution from mergers (red lines; the solid and dashed lines represent the same period distributions as in the top panel). Both observations and simulations shown here are restricted to white dwarfs with $T_{\rm eff} \geqslant 6000$ K.

similar; both predict a dominant peak around 0.6 $M_\odot$ with a tail toward higher masses. The main difference between the simulations using lognormal and flat period distributions is the number of systems that form through mergers (see Toonen et al. 2017 for a detailed discussion).

To see if mergers can help explain a significant portion of the massive white dwarfs in our sample, we compare our DA mass distribution against the predictions for blended populations of 70% white dwarfs from a 10 Gyr old disk population that evolved in isolation plus 30% single white dwarfs that formed through mergers. We picked 30% contribution from mergers, as this is the upper limit in the binary population synthesis calculations from Temmink et al. (2020).

Figure 15 in the bottom panel shows a comparison between our 100 pc DA white dwarf mass distribution against these blended populations, with the solid red line for the lognormal period distribution and the dotted line for the flat period distribution. Note that both observations and simulations shown here are restricted to white dwarfs with $T_{\rm eff} \geqslant 6000$ K. Just like in Figure 14, we normalize the synthetic populations to match the peak of the observed mass distribution at 0.59 $M_\odot$.

Even though the blended populations help increase the number of $M \sim 0.8\,M_\odot$ white dwarfs produced in the simulations and provide a better fit to the observational data in that mass range, the overall fit to the mass distribution is still problematic as these blended populations also produce more of the $M \sim 0.7$ and $>1\,M_\odot$ white dwarfs. The observed sample shows significant deficits for both $M \sim 0.7$ and $>1\,M_\odot$ white dwarfs compared to the model predictions.

4.2.2. Transverse Velocity Distribution

Merger populations can also reveal themselves through their kinematics. Double white dwarf merger products should have higher velocity dispersions because they would be part of an older population that is kinematically heated (Coutu et al. 2019; Cheng et al. 2020). Studying the kinematics of hot ($T_{\rm eff} >$ 13,000 K) DA white dwarfs from the PG survey and the SDSS DR4 white dwarf catalog (Eisenstein et al. 2006), Wegg & Phinney (2012) found that the transverse velocity dispersion decreases from $\sigma \sim 50$ km s^{-1} for 0.5 $M_\odot$ white dwarfs to $\sim$20 km s^{-1} for 0.8 $M_\odot$ white dwarfs. This is consistent with the expectations from single star evolution as the progenitors of lower mass white dwarfs belong to an older population where the disk heating is significant.

Wegg & Phinney (2012) did not find any high-mass white dwarfs traveling at >50 km s^{-1} in their young DA sample and concluded that the observed kinematics are consistent with the majority of high-mass white dwarfs forming through single star evolution. This is similar to the conclusions reached by Cheng et al. (2020), who estimate that the fraction of massive white dwarfs that form through double white dwarf mergers is around 10% in the 0.8–0.9 $M_\odot$ mass range. The exception to this is the massive DQ white dwarfs that display significantly larger transverse velocities, with 45% displaying velocities in excess of 50 km s^{-1} (Coutu et al. 2019). Hence, many of the massive DQ white dwarfs are likely produced through double white dwarf mergers.

Figure 16 shows the cumulative distribution of transverse velocities for our DA white dwarf sample split into three mass ranges, which correspond to the main peak in the mass distribution (0.5–0.7 $M_\odot$), the broad shoulder at 0.7–1 $M_\odot$, and very massive white dwarfs with $M > 1\,M_\odot$. The left and right panels show the distributions for the young and old DA samples with cooling ages (assuming single star evolution) younger than and older than 2 Gyr, respectively. The transverse velocities are based on Gaia DR2 parallaxes and proper motions.

Looking at the cumulative transverse velocity distribution for the younger DAs (left panel), we see the velocity dispersion

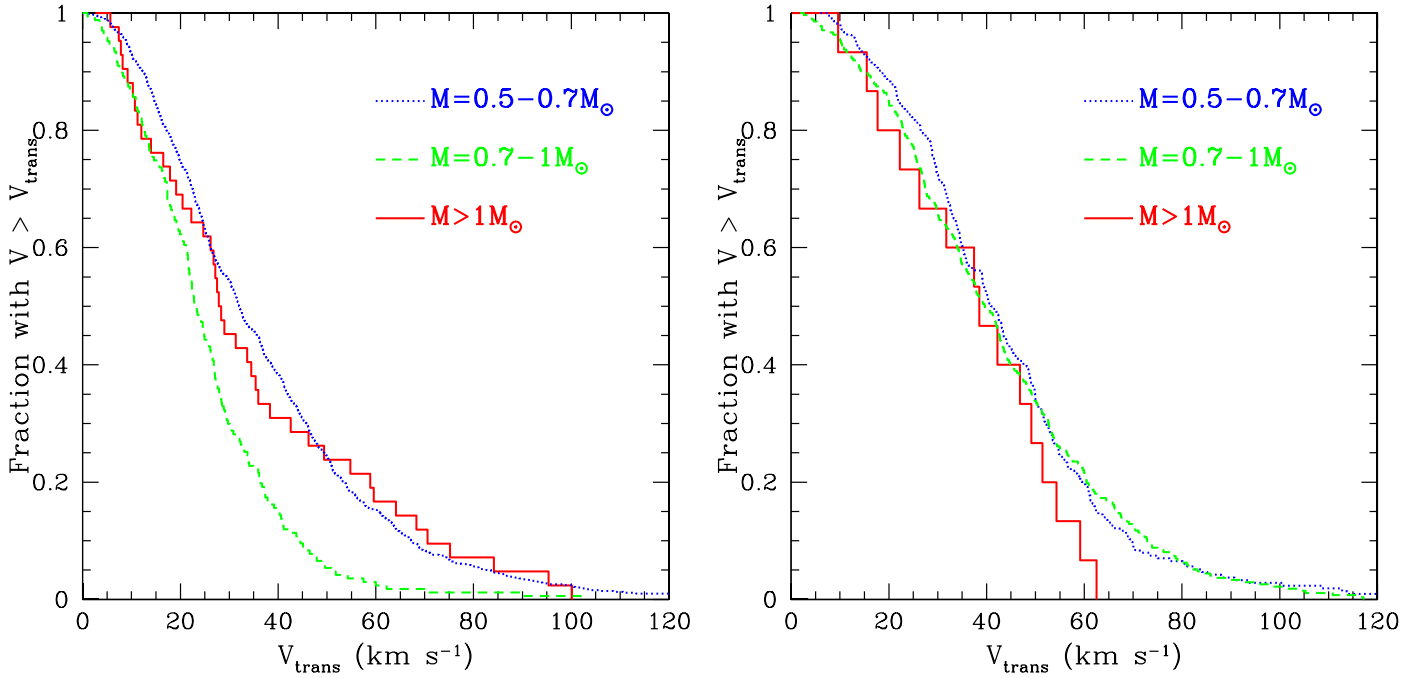

Figure 16. Cumulative distribution of transverse velocities for DA white dwarfs with cooling ages (assuming single star evolution) younger than (left panel) and older than (right panel) 2 Gyr and with M = 0.5–0.7, 0.7–1, and >1 $M_\odot$.

decreases for 0.7–1 $M_\odot$ white dwarfs compared to the 0.5–0.7 $M_\odot$ population. This is similar to what is seen in Wegg & Phinney (2012), which suggests that the mergers are unlikely to explain the number of 0.7–1 $M_\odot$ white dwarfs. On the other hand, the velocity distribution for the most massive white dwarfs with $M > 1\,M_\odot$ shows an excess of higher velocity objects compared to the 0.7–1 $M_\odot$ sample: 10 of the 44 hot DA white dwarfs with $M > 1\,M_\odot$ have $V_{\rm trans} > 50$ km s^{-1}. This would indicate a substantial contribution from mergers for the most massive white dwarfs and is consistent with the results from Temmink et al. (2020) and Cheng et al. (2020), who found that the fraction of >1 $M_\odot$ white dwarfs that come from mergers is ∼30%.

The transverse velocity distribution for the older DAs (right panel) is remarkably different. Here the distributions for the 0.5–0.7 and 0.7–1 $M_\odot$ white dwarfs are almost identical, but the velocity distribution for the $M > 1\,M_\odot$ cool DA sample in Figure 16 is significantly different: it is missing the high-velocity tail visible in the velocity distributions of the $M < 1\,M_\odot$ stars. This means that we are missing the oldest (and therefore the coolest) massive DA white dwarfs. Based on the velocity distributions for both hot and cool DAs, we can safely conclude that mergers cannot explain the relatively large numbers of $M \sim 0.8\,M_\odot$ white dwarfs, and we must look for an alternative explanation for these systems.

Another way to demonstrate this is through color–magnitude diagrams. Figure 17 displays synthetic color–magnitude diagrams for white dwarfs with a pure hydrogen atmosphere for a 10 Gyr old disk population with constant SFR and a Gaia magnitude limit of $G = 20$. The top panel assumes evolution in isolation, whereas the bottom panel includes single white dwarfs that form through mergers. A comparison with Figure 12 shows that none of the simulated populations, including the one with the mergers, can explain the observations.

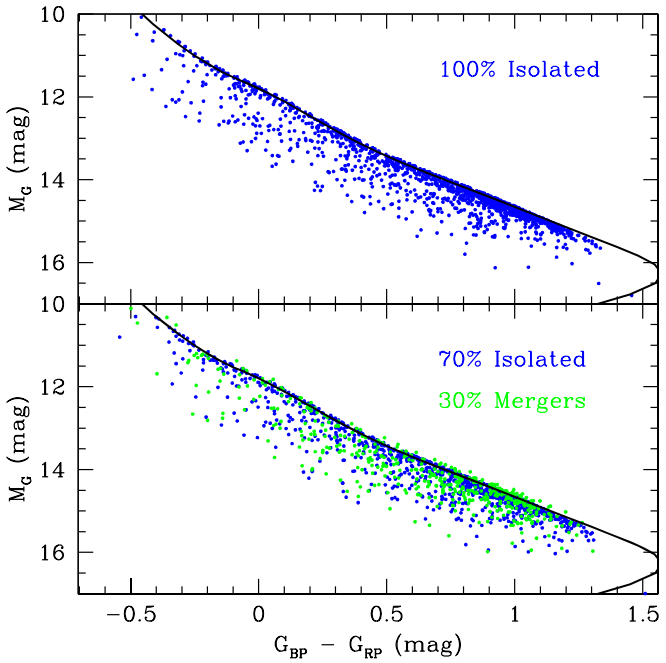

Figure 17. Synthetic color–magnitude diagrams for white dwarfs with a pure hydrogen atmosphere for a 10 Gyr old disk population and assuming a constant star formation rate. The top panel is for stars that evolved in isolation, whereas the bottom panel includes single white dwarfs that formed through mergers. Each panel displays the same number of stars as in Figure 12 for a fair comparison. The solid line shows the cooling sequence for a 0.6 $M_\odot$ pure hydrogen atmosphere white dwarf.

4.2.3. Crystallization

Tremblay et al. (2019) identified a pile-up in the cooling sequence of white dwarfs in Gaia color–magnitude diagrams and demonstrated that the latent heat of crystallization causes this pile-up. The release of latent heat results in a slowdown in the evolution of a white dwarf. Since massive white dwarfs

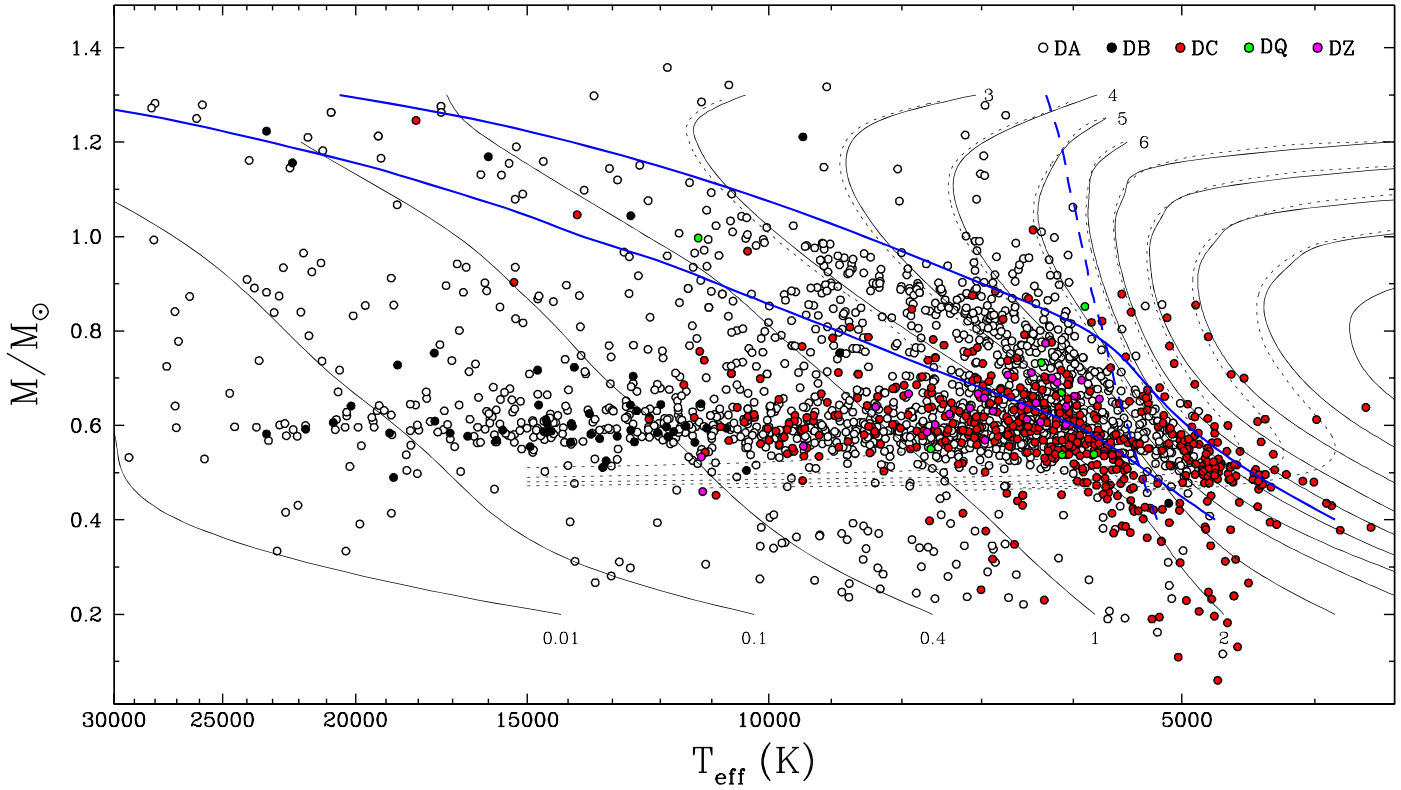

Figure 18. Stellar masses as a function of effective temperature for all spectroscopically confirmed white dwarfs in the 100 pc sample and the SDSS footprint. The parameters have been determined using photometric fits to the SDSS *u* and Pan-STARRS *grizy* photometry and Gaia DR2 parallaxes. Solid curves are theoretical isochrones, labeled in units of 10^9 yr, obtained from cooling sequences with C/O-core compositions, $q(\mathrm{He}) \equiv M(\mathrm{He})/M_* = 10^{-2}$, and $q(\mathrm{H}) = 10^{-4}$, while the dotted curves correspond to isochrones with the main-sequence lifetime taken into account. The lower blue solid curve indicates the onset of crystallization at the center of evolving models, while the upper one indicates the locations where 80% of the total mass has solidified. The dashed curve indicates the onset of convective coupling. Note that the low-mass DA white dwarfs in this diagram are most likely in unresolved degenerate binary systems, and their mass estimates may be erroneous because they were based on the assumption of a single star.

crystallize first, the effects of crystallization are most significant in their number distribution (see also Bergeron et al. 2019).

Bergeron et al. (2019) note that the most significant effect of crystallization is actually the Debye cooling phase, where the transition from the classical regime to the quantum regime occurs. In the quantum regime, the specific heat decreases with cooling, rapidly depleting the thermal energy reservoir of the star and making it essentially disappear from view as a black dwarf. Again, this is most significant for massive white dwarfs.

Our sample contains 44 DA white dwarfs with $T_{\rm eff} > 10{,}000$ K and cooling ages less than 2 Gyr, and only 15 DAs with $T_{\rm eff} =$ 6000–10,000 K and cooling ages more than 2 Gyr. A remaining question is whether the near absence of $M > 1\,M_\odot$ DA white dwarfs at cooler temperatures is due to those stars turning into massive DC stars or not.

Figure 18 shows the stellar masses as a function of temperature for all spectroscopically confirmed DA and non-DA white dwarfs in the 100 pc sample and the SDSS footprint. We restrict this figure to the objects with $T_{\rm eff} < 30{,}000$ K, where the photometric technique is the most reliable (Genest-Beaulieu & Bergeron 2019). Theoretical isochrones, with and without the main-sequence lifetime taken into account (Bergeron et al. 2001), are shown as solid and dotted curves, respectively. The nearly horizontal isochrones for massive white dwarfs at cooler temperatures indicate the Debye cooling regime, where the thermal reservoir of the star is rapidly depleted. This occurs below about $T_{\rm eff} = 6000$ K for $M \geqslant 1\,M_\odot$ white dwarfs.

The lower solid blue curve marks the region where crystallization starts at the center of the white dwarf, and with further cooling, the solidification front moves upward. By the time ~80% of the star has solidified, most of the latent heat would have been spent, and the upper solid blue curve marks this limit of 80% crystallization. The dashed curve marks the onset of convective coupling, when the convection zone first reaches into the degenerate interior, where all of the thermal energy of the star resides. Convective coupling significantly changes the cooling rates of white dwarfs, as evidenced by the sudden change in slope of the isochrones shown here.

Figure 18 demonstrates that the pile-up of massive white dwarfs seen in our 100 pc sample is clearly due to delays in cooling from the latent heat of crystallization. We see an enhanced number of white dwarfs between the two solid blue curves, where most of the latent heat of crystallization would have been released.

Just like the DA white dwarfs, the mass distribution for the non-DA stars is also dominated by 0.6 $M_\odot$ white dwarfs, with a small number of massive DC white dwarfs also present. Including trace amounts of hydrogen in our DC white dwarf fits leads to normal mass estimates for these stars, with no bias toward mass estimates lower than 0.5 or 0.4 $M_\odot$ at the cool end of the distribution.

Interestingly, there are only four massive DC white dwarfs with masses near 1 $M_\odot$. Three of these, J1621+0432, J1039−0325, and J1105+5225, are warmer than 13,000 K. Hence, to be classified DC, they must be strongly magnetic DAH or DBH

white dwarfs. The remaining object, J0930+0628, has $T_{\rm eff} = 6418 \pm 54$ K and $M = 1.01 \pm 0.02\,M_{\odot}$ assuming a composition of $\log{\rm H/He} = -3.2$. J0930+0628 appears to be the only genuine DC white dwarf more massive than 1 $M_{\odot}$.

Note that there are a number of cool and massive DA stars in the 40 pc sample of Limoges et al. (2015, see their Figure 21). However, the masses for those objects are mostly determined spectroscopically. For those in common (18 objects cooler than 8000 K and with $M > 0.8\,M_{\odot}$ based on spectroscopy), we find that the photometric mass is much smaller than the spectroscopic mass for all objects with spectroscopic masses above $0.9\,M_{\odot}$. This suggests that these objects are either double-degenerate systems or He-rich DAs. The fact that the photometric and spectroscopic temperature estimates agree for most of these objects would favor the latter explanation. Alternatively, a relatively weak magnetic field can also broaden the lines without displaying explicit Zeeman splitting in the low-resolution spectra, leading to erroneously high mass estimates. However, two of these objects, J1022+4600 and J1420+5322, have photometric mass estimates below $0.5\,M_{\odot}$, and therefore they are likely in binary systems.

4.2.4. Evolutionary Model Predictions

To check if the current evolutionary models (Fontaine et al. 2001) provide a reasonable match to the significance of the pile-up of $M \sim 0.8\,M_{\odot}$ white dwarfs in the 100 pc sample, we show the observed (top panel, similar to Figure 18) and the predicted (bottom panel) DA white dwarf mass and temperature distribution for a 10 Gyr old disk population with a constant star formation rate in Figure 19. These are the same evolutionary models used in Bergeron et al. (2019) and Tremblay et al. (2019).

Since our spectroscopic follow-up is severely incomplete beyond 6000 K, here we restrict our comparison to stars with $T_{\rm eff} \geqslant 6000$ K. Gaia's limiting magnitude also comes into play below this temperature. A 1 $M_{\odot}$ pure hydrogen atmosphere white dwarf is predicted to have $M_G = 15$ mag at 6000 K. Hence, the Gaia DR2 catalog suffers from incompleteness issues, even within 100 pc, for massive white dwarfs below this temperature. We limit our simulations to objects brighter than $G = 20$ mag to account for this bias.

A complication in the comparison and simulations shown in Figure 19 is the spectral evolution of white dwarfs: the atmospheric composition of a white dwarf changes throughout its evolution, due to several different mechanisms (see Blouin et al. 2018a for a detailed discussion). Given the white dwarf luminosity function, our sample is dominated by stars cooler than 10,000 K, where we also observe an increase in the ratio of non-DA to DA stars due to convective mixing. This means that a fraction of the DA white dwarfs turn into non-DAs below 10,000 K. We account for spectral evolution in our simulations by assuming one-third of all DAs below 10,000 K turn into non-DAs, essentially removing them from our simulated sample.

A comparison of the observed and predicted mass and temperature distributions of our 100 pc white dwarf sample shows that the synthetic population is significantly different from the observed one in two major ways: (1) there is no significant pile-up of $M \sim 0.8\,M_{\odot}$ white dwarfs, and (2) massive white dwarfs with $M > 1\,M_{\odot}$ do not disappear quickly enough.

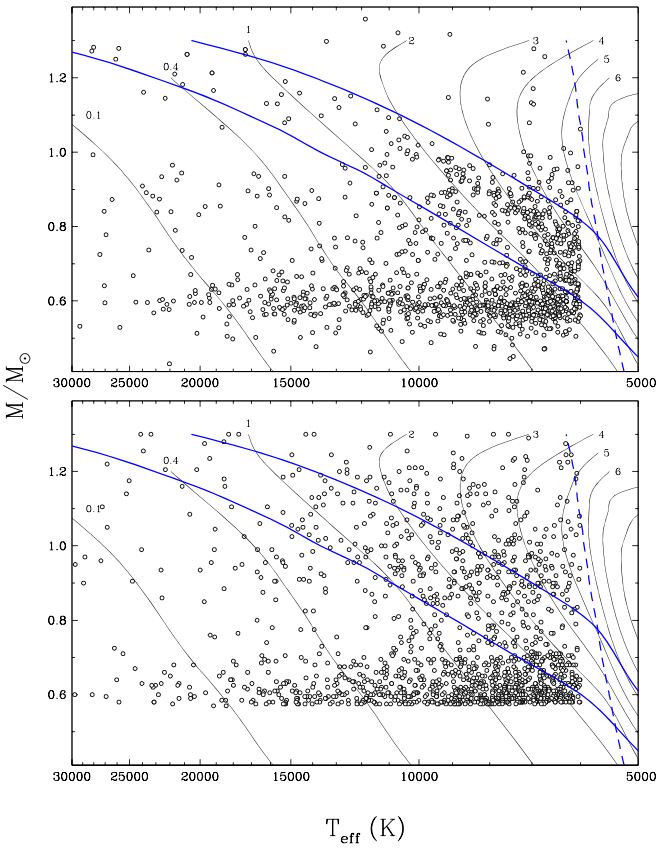

Figure 19. Observed (top, similar to Figure 18) and predicted (bottom) white dwarf mass and temperature distribution for a 10 Gyr old disk population with a constant star formation rate based on the current evolutionary models. Also shown are the same isochrones, crystallization, and convective coupling curves as in Figure 18. We limit this figure to stars hotter than 6000 K because our follow-up spectroscopy is severely incomplete below that temperature.

Even though the evolutionary models that include crystallization predict a slowdown in the cooling at the right location in the mass versus effective temperature diagram, where a pile-up of $\sim$0.8 $M_{\odot}$ white dwarfs is observed (Bergeron et al. 2019; Tremblay et al. 2019), the estimated delay in evolutionary times is clearly insufficient to produce any significant pile-up in the synthetic populations. In addition, the synthetic populations predict a significant population of massive white dwarfs at cooler temperatures that are simply absent in the observational sample.

Studying the number density and velocity distribution of massive white dwarfs on the Q branch, Cheng et al. (2019) arrived at a similar conclusion and found that the cooling delay from crystallization alone is not sufficient and suggested ^{22}Ne settling as a source of extra cooling delay. In addition, the effects of phase separation and ^{16}O sedimentation are currently not included in the evolutionary models (Fontaine et al. 2001). Additional factors such as the uncertain Coulomb plasma parameter at the liquid–solid phase transition, the C/O profile in the core, and the thickness of the surface hydrogen and helium layers also play a role in the cooling rates of these objects (Tremblay et al. 2019). Hence, our observational data clearly point to the onset of crystallization and its associated effects to explain the properties of the observed white dwarf mass distribution, but the current evolutionary models are missing important physics related to this process.

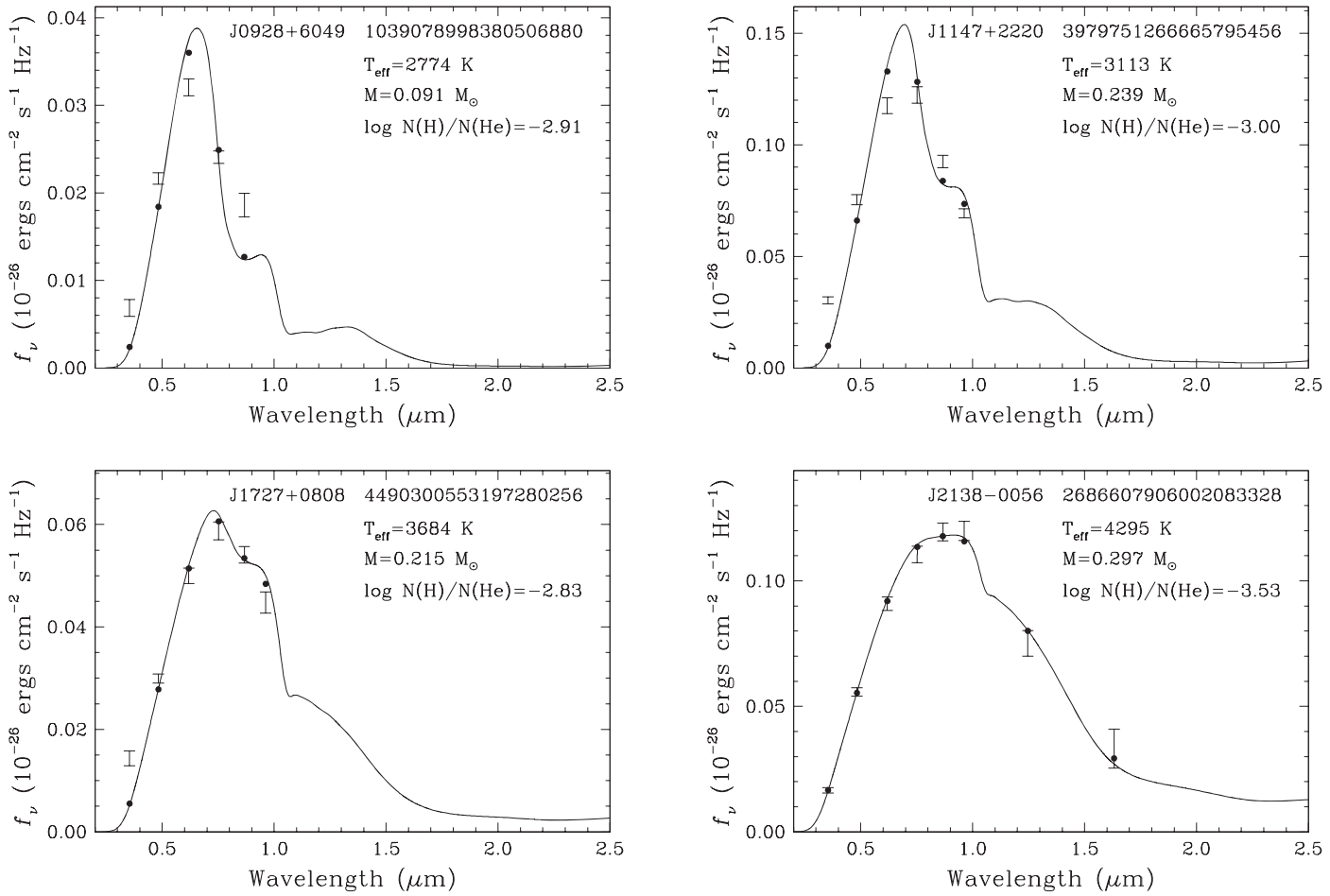

Figure 20. Fits to the spectral energy distributions of four new IR-faint white dwarfs identified in the 100 pc sample and the SDSS footprint. Solid lines show the monochromatic fluxes for the best-fit model for each star, and dots show the synthetic photometry of those models in each filter. Three of these objects, J0928+6049, J1147+2220, and J1727+0808, are spectroscopically confirmed DC white dwarfs. The remaining target, J2138−0056, currently lacks optical spectroscopy. All four targets show significant absorption in the near-infrared bands, z, y, J or H and are best explained by mixed H/He atmospheres.

4.3. IR-faint WDs

Among the 555 DC white dwarfs identified in our sample, there are a handful of known IR-faint white dwarfs that show optical and near-infrared flux deficits, presumably due to the CIA from molecular hydrogen. Even though we tend to refer to them as ultracool, implying they have temperatures below 4000 K, it is unclear if the majority of them are actually this cool, as mixed H/He atmosphere model fits indicate temperatures as high as ∼5500 K for some of them (Kilic et al. 2010; Gianninas et al. 2015).

For example, Blouin et al. (2018b) performed a detailed model atmosphere analysis of J0804+2239, a DZ white dwarf with significant absorption in the near-infrared. J0804+2239 is within 100 pc and included in our sample. Blouin et al. (2018b) find best-fit parameters of $T_{\rm eff} = 4970 \pm 100$ K, $\log g = 7.98 \pm 0.05$, and $\log{\rm H/He} = -1.6 \pm 0.2$. Hence, the term "IR-faint" is more appropriate for these objects.

We identify four additional white dwarfs with optical and near-infrared flux deficits in the 100 pc sample and the SDSS footprint. Figure 20 shows the spectral energy distributions for these four stars. Solid lines and dots show the monochromatic fluxes and the synthetic photometry for the best-fit model, respectively.

Three of these objects, J0928+6049, J1147+2220, and J1727+0808, are spectroscopically confirmed DC white dwarfs with SEDs that peak in the r or i band and with flux deficits visible in the Pan-STARRS z and y bands. The remaining object, J2138−0056, does not have follow-up spectroscopy, but it clearly shows a significant flux deficit in the near-infrared based on the UKIRT Infrared Deep Sky Survey (UKIDSS, Lawrence et al. 2007) JH photometry. If available, we also include the near-infrared photometry in our model fits. These fits indicate temperatures as low as 2774 K and hydrogen abundances of $\log{\rm H/He} \approx -3$. Note that this abundance corresponds to roughly the maximum intensity of the H_2–He CIA.

The intensity of CIA is controlled by the photospheric density and the H_2 abundance. The former decreases and the latter increases with an increase in the H/He ratio, which implies that there is a degeneracy between high and low hydrogen abundances below and above $\log{\rm H/He} \approx -3$ (Blouin et al. 2018b). For example, instead of the solution shown in Figure 20, the spectral energy distribution of J2138−0056 can also be fitted with a model that has $T_{\rm eff} = 4630$ K, $M = 0.429\,M_{\odot}$, and $\log{\rm H/He} = -2$. The model degeneracy is not an issue for the other three stars; the infrared flux deficit is much stronger in these stars, including the Pan-STARRS

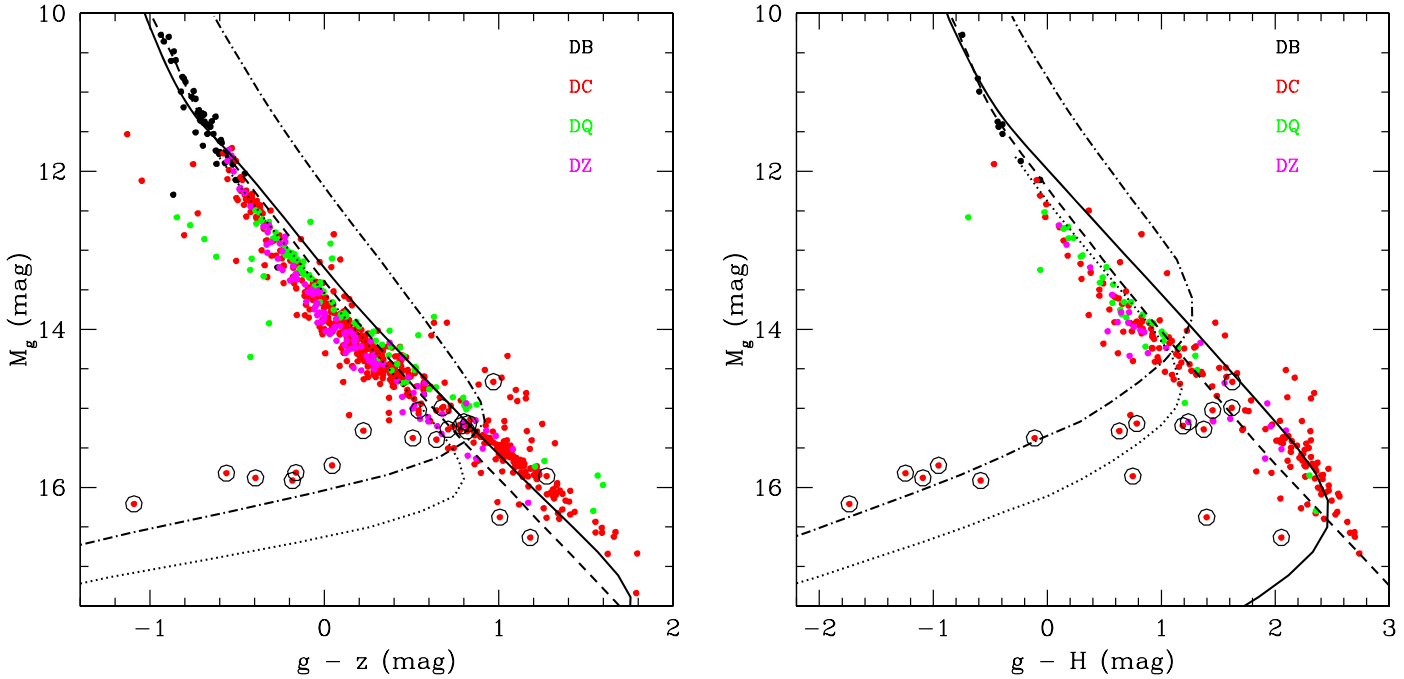

Figure 21. Near-infrared color–magnitude diagrams for the spectroscopically confirmed non-DA white dwarfs in the 100 pc sample and the SDSS footprint. IR-faint white dwarfs are marked by open circles. The solid, dashed, and dotted lines show the cooling sequences for 0.6 $M_{\odot}$ white dwarfs with pure H, pure He, and mixed H/He models with logH/He = −3, respectively. The dashed–dotted line shows the same mixed atmosphere models for a 0.2 $M_{\odot}$ white dwarf.

$z-$and Y-band photometry. Their spectral energy distributions require the maximum possible CIA to reproduce the flux deficit, so there is a unique solution for these objects.

Our mixed H/He atmosphere models barely replicate the broadband photometry for IR-faint white dwarfs, and no model can currently match the observed spectra. In addition, the relatively low temperature estimates force our model solutions to have relatively large radii to match the observed fluxes, which in turn require $M \sim 0.2\,M_{\odot}$ and log$g \sim 7$ for these objects. In fact, many of the previously known IR-faint white dwarfs with parallax measurements seem overluminous and require relatively large radii and small masses (e.g., Bergeron & Leggett 2002; Gianninas et al. 2015).

Using the clean sample of extremely low-mass (ELM, $M \sim 0.2\,M_{\odot}$) white dwarfs from Brown et al. (2020), we estimate that the local space density of "observed" ELM white dwarfs is 100–200 kpc^{-3} depending on the choice of Galactic scale length parameters (see Brown et al. 2016 for a detailed discussion). This means that there should be 0.4–0.8 ELM white dwarfs with $T_{\rm eff}$ = 9000–22,000 K within 100 pc of the Sun. Limiting the sample to the SDSS footprint lowers this estimate by about three times. To estimate the number of cool ELM white dwarfs, we use the evolutionary models for solar-metallicity progenitors from Istrate et al. (2016). We predict $N \sim 1$ ELM white dwarf with $4000 < T_{\rm eff} < 6000$ K, but we find 20 IR-faint white dwarfs in our sample. Hence, we can safely conclude that the majority of the IR-faint white dwarfs cannot be extremely low in mass.

Figure 21 shows near-infrared color–magnitude diagrams for the non-DA white dwarfs in our sample. The left panel is solely based on the Pan-STARRS data, whereas the right panel uses H-band data from the UKIDSS Large Area Survey and Kilic et al. (2010) for the majority of the IR-faint white dwarfs. We matched our list of non-DA white dwarfs with the Large Area Survey from the UKIDSS Data Release 11, and we found 244 objects with near-infrared observations. IR-faint white dwarfs, including the four newly identified systems presented here, are marked with open circles. We also show the cooling sequences for pure hydrogen, pure helium, and mixed H/He atmosphere white dwarfs, for reference.

Strikingly, 17 of the 20 IR-faint white dwarfs shown in this figure form a sequence in these color–magnitude diagrams. This is the first time such a sequence is clearly observed in a color–magnitude diagram. The cooling sequence for 0.2 $M_{\odot}$ white dwarfs with logH/He = −3 comes closest to matching this sequence, but the match is not perfect in either diagram.

The IR-faint white dwarf sequence is connected to a region in the M_g versus $g - z$ color–magnitude diagram where the number of DC white dwarfs appears to be low. There are a significant number of DC white dwarfs blueward of $g - z = 0.5$ mag, and there are also a large number of them redward of $g - z = 0.9$ mag, but the DC white dwarf population is significantly depleted between these two colors. This color range corresponds to ≈5000–6000 K for 0.6 $M_{\odot}$ pure hydrogen white dwarfs. This is the same temperature range where Bergeron et al. (1997, 2001) found depleted numbers of helium-rich stars compared to their hydrogen-rich counterparts (see also Blouin et al. 2019). This is likely related to the spectral evolution of white dwarfs and the transformation of helium-rich white dwarfs to a hydrogen-rich composition, and vice versa, through some yet-unexplained phenomenon (Malo et al. 1999; Chen & Hansen 2012).

We interpret the observed sequence of IR-faint white dwarfs in Figure 21 as a cooling sequence of white dwarfs with mixed H/He atmospheres. That the sequence is so tight indicates that these stars probably have similar hydrogen abundances, around logH/He = −3. In addition, the analysis by Bergeron et al. (2019) indicates that some of the warmer DC stars (above 6000 K) have such trace amounts of hydrogen in their

atmospheres. Hence, it is possible that such an IR-faint white dwarf sequence due to CIA is unavoidable.

Clearly, a large fraction of the warmer DC white dwarfs turn into hydrogen-rich DC stars below 5000 K, otherwise we would see a lot more objects with CIA absorption, but a few of those likely retain their helium-dominated atmospheres and end up on the IR-faint white dwarf cooling sequence instead.

In summary, we see a mix of hydrogen- and helium-atmosphere white dwarfs above 6000 K. These are the DA and DC/DQ/DZ white dwarfs, respectively. Since hydrogen lines disappear below 5000 K, we have to rely on other indicators for composition, like the presence of metals, the red wing of the Lyα line, and CIA. There are three possible outcomes for cool DC white dwarfs below 5000 K: (1) The color–magnitude diagram suggests that most cool white dwarfs evolve as pure hydrogen atmospheres through some unknown process. (2) Some evolve as IR-faint white dwarfs on a cooling sequence with hydrogen abundances that are typical of some of the hotter DC and DZ white dwarfs, whose origin is likely convectively mixed DAs. (3) Some also evolve as DC white dwarfs with almost pure helium atmospheres, with hydrogen abundances low enough to produce no visible CIA signatures. The progenitors of the latter likely have very little hydrogen, potentially DQ stars or cooled-off DB stars.

5. Conclusions

We present the results from a follow-up spectroscopy survey of the 100 pc white dwarf sample in the SDSS footprint. Our follow-up is complete for 83% of the white dwarfs hotter than 6000 K. We perform a detailed model atmosphere analysis of each white dwarf and use this sample to constrain the DA white dwarf mass distribution, which displays an extremely narrow peak at 0.59 $M_{\odot}$ and a broad shoulder up to 0.9 $M_{\odot}$.

Surprisingly, the number of massive white dwarfs remains roughly constant in the 0.7–0.9 $M_{\odot}$ range. The predictions from single and binary population synthesis studies fail to match this overabundance of massive white dwarfs. The location of the pile-up of $\sim$0.8 $M_{\odot}$ white dwarfs in the mass versus temperature diagrams and the disappearance of $M > 1\,M_{\odot}$ white dwarfs from these samples are consistent with the expectations for crystallization and related effects.

The former is explained by a delay in cooling that is due to the release of the latent heat of crystallization, whereas the latter is explained by enhanced cooling in the quantum regime where massive white dwarfs quickly disappear from the sample. However, we find that the current evolutionary models are unable to match the significance of the pile-up of $\sim$0.8 $M_{\odot}$ and the sudden disappearance of the more massive stars.

We suggest that additional cooling delays from ^{16}O sedimentation upon crystallization and ^{22}Ne gravitational settling likely play a significant role in the evolution of white dwarfs, and that convective coupling may lead to even faster cooling than currently predicted.

We also discuss the prevalence of IR-faint white dwarfs in the 100 pc sample and the SDSS footprint. We find 20 IR-faint white dwarfs that show significant flux deficits in the optical or near-infrared. We demonstrate that these white dwarfs form a sequence in color–magnitude diagrams. In addition, the IR-faint white dwarf sequence seems to be connected to a region in the color–magnitude diagrams where the number of helium-dominated atmosphere white dwarfs is low. This suggests that the transition of helium-rich white dwarfs into hydrogen-rich atmospheres, and vice versa, may also explain the appearance of IR-faint white dwarfs, and that IR-faint white dwarfs likely have mixed H/He atmospheres.

This work is supported in part by the NSF under grant AST-1906379, the NSERC Canada, the Fund FRQ-NT (Québec), and the Smithsonian Institution. S.B. acknowledges support from the Laboratory Directed Research and Development program of Los Alamos National Laboratory under project number 20190624PRD2.

We thank B. Kunk, E. Martin, and A. Milone for their assistance with observations obtained at the MMT Observatory, a joint facility of the Smithsonian Institution and the University of Arizona.

This work is based on observations obtained at the MDM Observatory, operated by Dartmouth College, Columbia University, Ohio State University, Ohio University, and the University of Michigan. We thank J. Rupert for obtaining the MDM data as part of the OSMOS queue.

This research is based in part on observations obtained with the Apache Point Observatory 3.5 m telescope, which is owned and operated by the Astrophysical Research Consortium.

This work is based on observations obtained at the Gemini Observatory, which is operated by the Association of Universities for Research in Astronomy, Inc., under a cooperative agreement with the NSF on behalf of the Gemini partnership: the National Science Foundation (United States), National Research Council (Canada), CONICYT (Chile), Ministerio de Ciencia, Tecnología e Innovación Productiva (Argentina), Ministério da Ciência, Tecnologia e Inovação (Brazil), and Korea Astronomy and Space Science Institute (Republic of Korea).

Facilities: MMT (Blue Channel spectrograph), FLWO:1.5 m (FAST spectrograph), Gemini (GMOS spectrograph), APO (DIS), MDM (OSMOS).

Appendix

The ADL query used to select our sample of 100 pc white dwarfs in the SDSS footprint is given below.

```
SELECT g.source_id, g.ra, g.dec, parallax,
parallax_over_error, pmra, pmra_error, pmdec,
pmdec_error, phot_g_mean_mag, phot_g_mean_
flux_over_error, phot_bp_mean_mag, phot_bp_
mean_flux_over_error, phot_rp_mean_mag, phot_
rp_mean_flux_over_error, phot_g_mean_mag + 5.0*
log10(parallax/100.0) AS M_G, s.ra,s.dec,
u_mag, u_mag_error, g_mag, g_mag_error, r_mag,
r_mag_error, i_mag, i_mag_error, z_mag, z_mag_
error, clean_flag
FROM gaiadr2.gaia_source AS g, gaiadr1.
sdssdr9_original_valid AS s, gaiadr2.sdssdr9_
best_neighbour AS xs
WHERE g.source_id=xs.source_id AND s.sdssdr9_
oid=xs.sdssdr9_oid AND parallax>10.0
AND parallax_over_error >10.0 AND phot_bp_
mean_flux_over_error >10
AND phot_rp_mean_flux_over_error >10AND astro-
metric_n_good_obs_al >5
AND (SQRT(astrometric_chi2_al/(astrometric_
n_good_obs_al−5.0)) <1.2 OR
```

```
  SQRT(astrometric_chi2_al/(astrometric_
n_good_obs_al−5.0))    <1.2*exp(-0.2*(phot_
g_mean_mag−19.5)))
  AND phot_bp_rp_excess_factor BETWEEN 1.0 +
(0.03*POWER(phot_bp_mean_mag−phot_rp_mean_
mag,  2.0))AND  1.3  +  (0.06*POWER(phot_bp_
mean_mag−phot_rp_mean_mag, 2.0))
  AND phot_g_mean_mag + 5.0*log10(parallax/
100.0) > (3.333333*(phot_bp_mean_mag−phot_rp_
mean_mag) + 8.333333)
```

ORCID iDs

Mukremin Kilic https://orcid.org/0000-0001-6098-2235
P. Bergeron https://orcid.org/0000-0003-2368-345X
Alekzander Kosakowski https://orcid.org/0000-0002-9878-1647
Warren R. Brown https://orcid.org/0000-0002-4462-2341
Marcel A. Agüeros https://orcid.org/0000-0001-7077-3664
Simon Blouin https://orcid.org/0000-0002-9632-1436

References

Ahn, C. P., Alexandroff, R., Allende Prieto, C., et al. 2012, ApJS, 203, 21
Bergeron, P., Dufour, P., Fontaine, G., et al. 2019, ApJ, 876, 67
Bergeron, P., & Leggett, S. K. 2002, ApJ, 580, 1070
Bergeron, P., Leggett, S. K., & Ruiz, M. T. 2001, ApJS, 133, 413
Bergeron, P., Ruiz, M. T., & Leggett, S. K. 1997, ApJS, 108, 339
Bergeron, P., Wesemael, F., & Fontaine, G. 1991, ApJ, 367, 253
Blouin, S., & Dufour, P. 2019, MNRAS, 490, 4166
Blouin, S., Dufour, P., & Allard, N. F. 2018a, ApJ, 863, 184
Blouin, S., Dufour, P., Allard, N. F., & Kilic, M. 2018b, ApJ, 867, 161
Blouin, S., Dufour, P., Thibeault, C., & Allard, N. F. 2019, ApJ, 878, 63
Briggs, G. P., Ferrario, L., Tout, C. A., Wickramasinghe, D. T., & Hurley, J. R. 2015, MNRAS, 447, 1713
Brown, W. R., Kilic, M., Kenyon, S. J., & Gianninas, A. 2016, ApJ, 824, 46
Brown, W. R., Kilic, M., Kosakowski, A., et al. 2020, ApJ, 889, 49
Chambers, K. C., Magnier, E. A., Metcalfe, N., et al. 2016, arXiv:1612.05560
Chen, E. Y., & Hansen, B. M. S. 2012, ApJL, 753, L16
Cheng, S., Cummings, J. D., & Ménard, B. 2019, ApJ, 886, 100
Cheng, S., Cummings, J. D., Ménard, B., & Toonen, S. 2020, ApJ, 891, 160
Coutu, S., Dufour, P., Bergeron, P., et al. 2019, ApJ, 885, 74
Cummings, J. D., Kalirai, J. S., Tremblay, P. E., Ramirez-Ruiz, E., & Choi, J. 2018, ApJ, 866, 21
Dufour, P., Blouin, S., Coutu, S., et al. 2017, in ASP Conf. Ser. 509, 20th European White Dwarf Workshop, 509, ed. P.-E. Tremblay, B. Gänsicke, & T. Marsh (San Francisco, CA: ASP), 3
Eisenstein, D. J., Liebert, J., Harris, H. C., et al. 2006, ApJS, 167, 40
El-Badry, K., Rix, H.-W., & Weisz, D. R. 2018, ApJL, 860, L17
Fabricant, D., Cheimets, P., Caldwell, N., & Geary, J. 1998, PASP, 110, 79
Fontaine, G., Brassard, P., & Bergeron, P. 2001, PASP, 113, 409
Gaia Collaboration, Babusiaux, C., van Leeuwen, F., et al. 2018, A&A, 616, A10
Genest-Beaulieu, C., & Bergeron, P. 2019, ApJ, 882, 106
Gentile Fusillo, N. P., Tremblay, P.-E., Gänsicke, B. T., et al. 2019, MNRAS, 482, 4570
Giammichele, N., Bergeron, P., & Dufour, P. 2012, ApJS, 199, 29
Gianninas, A., Bergeron, P., & Ruiz, M. T. 2011, ApJ, 743, 138
Gianninas, A., Curd, B., Thorstensen, J. R., et al. 2015, MNRAS, 449, 3966
Green, R. F., Schmidt, M., & Liebert, J. 1986, ApJS, 61, 305
Holberg, J. B. 2009, JHA, 40, 137
Holberg, J. B., & Bergeron, P. 2006, AJ, 132, 1221
Holberg, J. B., Oswalt, T. D., Sion, E. M., & McCook, G. P. 2016, MNRAS, 462, 2295
Hollands, M. A., Tremblay, P. E., Gänsicke, B. T., Gentile-Fusillo, N. P., & Toonen, S. 2018, MNRAS, 480, 3942
Hurley, J. R., Pols, O. R., & Tout, C. A. 2000, MNRAS, 315, 543
Hurley, J. R., Tout, C. A., & Pols, O. R. 2002, MNRAS, 329, 897
Istrate, A. G., Marchant, P., Tauris, T. M., et al. 2016, A&A, 595, A35
Jiménez-Esteban, F. M., Torres, S., Rebassa-Mansergas, A., et al. 2018, MNRAS, 480, 4505
Kawka, A. 2020, arXiv:2001.10672
Kepler, S. O., Pelisoli, I., Koester, D., et al. 2019, MNRAS, 486, 2169
Kilic, M., Bédard, A., Bergeron, P., & Kosakowski, A. 2020, MNRAS, 493, 2805
Kilic, M., Hambly, N. C., Bergeron, P., Genest-Beaulieu, C., & Rowell, N. 2018, MNRAS, 479, L113
Kilic, M., Leggett, S. K., Tremblay, P. E., et al. 2010, ApJS, 190, 77
Kilic, M., Munn, J. A., Harris, H. C., et al. 2006, AJ, 131, 582
Kleinman, S. J., Kepler, S. O., Koester, D., et al. 2013, ApJS, 204, 5
Koester, D., & Kepler, S. O. 2019, A&A, 628, A102
Kowalski, P. M., & Saumon, D. 2006, ApJL, 651, L137
Lawrence, A., Warren, S. J., Almaini, O., et al. 2007, MNRAS, 379, 1599
Liebert, J., Bergeron, P., & Holberg, J. B. 2005, ApJS, 156, 47
Limoges, M. M., Bergeron, P., & Lépine, S. 2015, ApJS, 219, 19
Lindegren, L., Hernández, J., Bombrun, A., et al. 2018, A&A, 616, A2
Luyten, W. J. 1976, LHS (Luyten half-second) Catalogue (Minneapolis, MN: Univ. Minnesota Press)
Malo, A., Wesemael, F., & Bergeron, P. 1999, ApJ, 517, 901
Marsh, T. R., Dhillon, V. S., & Duck, S. R. 1995, MNRAS, 275, 828
Martini, P., Stoll, R., Derwent, M. A., et al. 2011, PASP, 123, 187
McCook, G. P., & Sion, E. M. 1987, ApJS, 65, 603
McCook, G. P., & Sion, E. M. 1999, ApJS, 121, 1
Napiwotzki, R., Christlieb, N., Drechsel, H., et al. 2001, AN, 322, 411
Press, W. H., Flannery, B. P., & Teukolsky, S. A. 1986, Numerical Recipes. The Art of Scientific Computing (Cambridge: Cambridge Univ. Press)
Rolland, B., Bergeron, P., & Fontaine, G. 2018, ApJ, 857, 56
Salpeter, E. E. 1955, ApJ, 121, 161
Schmidt, G. D., Weymann, R. J., & Foltz, C. B. 1989, PASP, 101, 713
Temmink, K. D., Toonen, S., Zapartas, E., Justham, S., & Gänsicke, B. T. 2020, A&A, 636, A31
Tokarz, S. P., & Roll, J. 1997, in ASP Conf. Ser. 125, adass VI, 125, ed. G. Hunt & H. E. Payne (San Francisco, CA: ASP), 140
Tonry, J. L., Stubbs, C. W., Lykke, K. R., et al. 2012, ApJ, 750, 99
Toonen, S., Hollands, M., Gänsicke, B. T., & Boekholt, T. 2017, A&A, 602, A16
Tremblay, P.-E., Fontaine, G., Fusillo, N. P. G., et al. 2019, Natur, 565, 202
Wegg, C., & Phinney, E. S. 2012, MNRAS, 426, 427
Zuckerman, B., Koester, D., Melis, C., Hansen, B. M., & Jura, M. 2007, ApJ, 671, 872